JAMES | Journal of Advances in Modeling Earth Systems®

RESEARCH ARTICLE
10.1029/2024MS004560

Key Points:

- Mesoscale eddies backscatter kinetic energy to scales resolvable by non-eddying ocean models
- A stochastic kinetic energy backscatter parameterization is developed for non-eddying ocean models

Correspondence to:
I. Grooms,
ian.grooms@colorado.edu

Citation:
Grooms, I., Agarwal, N., Marques, G., Pegion, P. J., & Yassin, H. (2025). The stochastic GM + E closure: A framework for coupling stochastic backscatter with the Gent and McWilliams parameterization. *Journal of Advances in Modeling Earth Systems*, *17*, e2024MS004560. https://doi.org/10.1029/2024MS004560

Received 9 JUL 2024
Accepted 3 MAY 2025

The Stochastic GM + E Closure: A Framework for Coupling Stochastic Backscatter With the Gent and McWilliams Parameterization

I. Grooms[1], N. Agarwal[2,3], G. Marques[4], P. J. Pegion[3], and H. Yassin[1]

[1]Department of Applied Mathematics, University of Colorado, Boulder, CO, USA, [2]Cooperative Institute for Research in Environmental Sciences, University of Colorado Boulder, Boulder, CO, USA, [3]NOAA Physics Sciences Lab, Boulder, CO, USA, [4]Climate and Global Dynamics Laboratory, National Center for Atmospheric Research, Boulder, CO, USA

Abstract Ocean general circulation models (OGCMs) are often used at horizontal resolutions that preclude the appearance of mesoscale eddies. The ocean mesoscale constitutes a significant component of ocean variability, and OGCMs whose resolutions are too coarse to represent the mesoscale are necessarily lacking this variability. In addition to being variable, the ocean mesoscale also induces variability on larger scales that could be resolved on a coarse grid, but coarse OGCMs often lack this variability too. This paper develops a stochastic parameterization that adds small increments to an OGCM's lateral velocity field, which excites natural modes of variability in the model. The rate at which these velocity increments add energy to the flow is tied to the rate at which the Gent-McWilliams parameterization—a popular parameterization of the effect of mesoscale eddies on tracer transport—removes potential energy from the resolved scales. The stochastic parameterization is implemented in a non-eddying OGCM, where it is shown to increase the variability significantly.

Plain Language Summary Models used to simulate global ocean currents often have horizontal resolutions that are too low to see ocean mesoscale eddies, which are to the ocean what weather systems are to the atmosphere. These ocean eddies jostle each other and the larger-scale currents in a chaotic manner, leading to variability on scales that could, in principle, be resolved by ocean models. But since the ocean models don't actually include the eddies themselves, the currents they resolve won't be jostled about realistically unless we enhance the models by adding a realistic description of the effects of the eddies that the models can't see. This paper develops such a description, called a stochastic parameterization. The eddies get their energy by taking some from the larger scales - the ones that the ocean model can resolve - and there is already a well-established representation of how the eddies remove energy from the large scales. The new stochastic parameterization developed here takes some of the energy that the eddies remove from the larger, resolved scales and recycles it back into the simulation in a random fashion that mimics the chaotic action of the unresolved eddies.

1. Introduction

Ocean General Circulation Models (OGCMs) are used for a range of tasks, from simulating past and future climates to ensemble forecasting and data assimilation. However, simulating the global ocean at high resolution is computationally expensive. When this computational cost is compounded by the need to simulate over long time frames, to run ensembles, or to track additional variables like those in marine ecosystem and chemistry models, the cost can be prohibitive. As a result, OGCMs used for these purposes often rely on a coarser resolution, typically around 1° or more across the ocean. Because of this limitation, these models cannot resolve mesoscale eddies, and their effects must be parameterized.

Mesoscale eddies transport tracers and momentum, and directly influence the exchange of heat, carbon, and momentum with the atmosphere. The Gent-McWilliams (GM) framework is widely used to parameterize the advective transport of tracers by mesoscale eddies (Gent et al., 1995; Gent & McWilliams, 1990); it is often used in combination with an isopycnal or isoneutral diffusion model for the diffusive transport of tracers by mesoscale eddies (Redi, 1982). Broadly speaking, the GM framework introduces a velocity field in the tracer equations that acts to flatten isopycnals. This flattening of isopycnals removes potential energy from the resolved flow, mimicking the extraction of large-scale potential energy by the nonlinear baroclinic instability that drives mesoscale eddies.

The ocean mesoscale constitutes a significant component of ocean variability, and OGCMs whose resolutions are too coarse to represent the mesoscale are necessarily lacking this variability. In addition to being variable, the ocean mesoscale also induces variability on larger scales that can be resolved on a coarse grid, but coarse OGCMs often lack this variability too. This leads to reduced variability in air-sea heat fluxes (e.g., Agarwal et al., 2023; Bishop et al., 2017). In the context of ensemble forecasting and data assimilation this can lead to under-dispersed ensembles.

Stochastic parameterization is a common approach to increasing variability in weather and climate models (Berner et al., 2017; Leutbecher et al., 2017). Two approaches from this community are sufficiently general to apply to OGCMs with minimal modifications: Stochastically Perturbed Parameterization Tendencies (SPPT) and Stochastically Perturbed Parameters (SPP). SPPT multiplies one or more parameterization tendencies by a random field, while SPP multiplies one or more parameters within a parameterization by a random field. The distribution of the random field is often centered on one, with no (or small) probability of changing sign, and with tunable spatial and temporal correlations. SPPT and SPP have been used in the OGCM context by P. D. Williams (2012); Andrejczuk et al. (2016), and Juricke et al. (2017). Grooms and Kleiber (2019) took a data-driven approach to SPP for the GM parameterization and found that it was not possible to construct a random field for use with SPP that would come close to matching the diagnosed mesoscale-eddy tracer tendency.

Rather than simply perturb existing parameterizations, other authors have taken an ab initio approach to developing stochastic parameterizations for unresolved processes. For example, Grooms (2016) developed a non-Gaussian stochastic GM parameterization that replaces (rather than perturbs) the deterministic GM parameterization of buoyancy flux with a stochastic model. Brankart (2013) developed a stochastic parameterization modeling the impact of unresolved temperature and salinity perturbations on the resolved density field. P. Williams et al. (2016) added a stochastic source to the temperature tendency of their model to achieve an effect on the resolved density field similar to the effect of the Brankart parameterization. A different stochastic parameterization of the effect of unresolved temperature fluctuations on resolved density was developed by Stanley et al. (2020) and tested by Kenigson et al. (2022) and Agarwal et al. (2023).

Kinetic energy backscatter parameterizations are another means of increasing variability in a low-resolution model (Berner et al., 2009). In the context of coarse OGCMs, backscattering energy from unresolved scales is not merely convenient, it is physically relevant: Loose, Bachman, et al. (2023) diagnosed the transfer of energy across scales in an idealized high-resolution ocean model and found, inter alia, that the mesoscale transfers kinetic energy back to scales larger than the mesoscale, that is, scales that could be resolved on a coarse OGCM grid. Several backscatter schemes have been developed in the context of OGCMs (e.g., Bachman, 2019; Bagaeva et al., 2024; Grooms, 2023; Jansen, Held, et al., 2015; Juricke, Danilov, Koldunov, Oliver, Sein, et al., 2020; Juricke, Danilov, Koldunov, Oliver, & Sidorenko, 2020; Zanna & Bolton, 2020). Many of these are aimed at eddy-permitting resolutions and use deterministic schemes that amplify existing variability; as a result, they may not be well suited to coarse OGCMs that completely fail to represent mesoscale eddies.

A stochastic backscatter scheme for OGCMs was developed by Storto and Andriopoulos (2021), who adapted the atmospheric Stochastic Kinetic Energy Backscatter (SKEB) scheme from Berner et al. (2009) to an ocean modeling context. They developed their scheme in the context of a high-resolution (1.6 km) regional ocean model, and its suitability for coarse OGCMs remains unexplored. O'Kane et al. (2023) implemented a stochastic backscatter parameterization in a 1° configuration of the ACCESS-OM2 model by multiplying the resolved lateral momentum fluxes by a random field. Their use of a multiplicative random field is akin to SPP and SPPT, but in this case the perturbations are not applied to a parameterization tendency (SPPT) or to a parameter within a parameterization (SPP); rather, the resolved momentum flux is perturbed to model the momentum transport by unresolved mesoscale eddies.

Here, we develop a stochastic kinetic energy backscatter parameterization for coarse OGCMs inspired by the GM + E closure of Bachman (2019) and the SKEB scheme of Berner et al. (2009). The SKEB scheme sets the rate of kinetic energy backscatter to some fraction of the dissipation rates affected by lateral viscosity and other parameterizations. The GM + E scheme makes a similar choice, but one more appropriate to the OGCM context: the backscatter rate is set proportional to the rate of potential energy dissipation affected by the GM parameterization. The original GM + E scheme affects this backscatter through a negative viscosity. However, a negative Laplacian viscosity coefficient can cause problems if it is not tamed at small scales by a biharmonic viscosity (cf. Grooms, 2023; Jansen, Held, et al., 2015). Rather than add a biharmonic viscosity, the original GM + E scheme

separates the backscatter so that it acts only on the barotropic component of the velocity field (i.e., the depth-averaged part), while the baroclinic velocity still feels a positive (i.e., dissipative) viscosity. The stochastic GM + E scheme developed here retains the decision to let the backscatter rate be proportional to the rate of potential energy dissipation affected by the GM parameterization, but accomplishes the backscatter through a stochastic approach similar to the SKEB scheme.

The stochastic GM + E parameterization is presented in Section 2. The model configuration and experimental design are presented in Section 3, and the results are presented in Section 4. A concluding discussion is offered in Section 5.

2. Velocity Increment Structure

The stochastic GM + E closure can be thought of as adding a stochastic forcing term to the momentum equations of the ocean model representing the divergence of stresses associated with the unresolved mesoscale, but practically it is implemented by adding an increment $\Delta \boldsymbol{u}$ to the (lateral) velocity field between model time steps. This section details the nature of these increments. The velocity increments are defined by

$$\Delta u = -M_{\text{taper}}(x,y)\partial_y \psi(x,y,z,t), \tag{1a}$$

$$\Delta v = M_{\text{taper}}(x,y)\partial_x \psi(x,y,z,t). \tag{1b}$$

In the above equations M_{taper} is a nondimensional taper function that smoothly tapers the velocity increment to zero near coastlines, and ψ is a random field with dimensions of length squared over time. The construction implies that, except near the coasts, the velocity increments are nondivergent, which limits the generation of internal waves.

The construction of the streamfunction ψ is detailed below. It is not constant along the lateral boundaries, which means that without the taper function M_{taper} the stochastic velocity increment would have a nonzero component into solid boundaries. This could be arbitrarily set to zero on the boundaries, but then it would induce a strong divergence (and, therefore, a large vertical velocity) in grid cells adjacent to the boundaries. The taper function is imposed to avoid this; still, the presence of the taper does induce some weak divergence near the boundaries.

The streamfunction ψ is constructed as the product of a depth-independent amplitude A, a vertical profile ϕ, and a random field χ

$$\psi(x,y,z,t) = A(x,y,t)\phi(x,y,z,t)\chi(x,y,t). \tag{2}$$

The random field χ has dimensions of length, the vertical structure ϕ is nondimensional, and the amplitude A has dimensions of length over time. The zonal velocity increment from this construction has the form

$$\Delta u = -M_{\text{taper}}[A\phi\partial_y\chi + A\chi\partial_y\phi + \phi\chi\partial_y A]. \tag{3}$$

The idea is that A should control the amplitude of the backscatter while ϕ should control its distribution across depth. For this to be accurate, A and ϕ must vary over lateral length scales that are much longer than χ so that the last two terms in Equation 3 are small compared to the first one. We consider each of M_{taper}, χ, A, and ϕ in the subsections below.

2.1. Increment Taper

The taper function M_{taper} is constructed by the following steps.

1. The taper is set to one in wet grid cells and to zero on land.
2. The taper is set to zero in all cells that are adjacent to cells that are already zero. This step is performed twice.
3. The taper is smoothed by the application of a nine-point moving average filter with stencil

$$\frac{1}{16}\begin{bmatrix}1 & 2 & 1\\ 2 & 4 & 2\\ 1 & 2 & 1\end{bmatrix}. \tag{4}$$

This step is performed twice. After each pass of the filter, the taper is again set to zero on land.

This construction creates a transition layer that is four grid points wide over which the stochastic velocity increments are tapered to zero. The width of the transition layer can be tuned by changing the number of times that steps 2 and 3 are repeated. Future work may explore the use of separate taper functions for the two components of velocity, since this would enable the increment normal to the boundary to be tapered separately from the increment parallel to the boundary.

2.2. Random Field

The random field $\chi(x, y, t)$ is constructed so that if ϕ and A did not vary horizontally, then, away from the boundaries, the mean kinetic energy of the velocity increments would be $A^2\phi^2$. (Here and throughout, the term "kinetic energy" is used as a shorthand for kinetic energy per unit mass.) Following Berner et al. (2009) we construct χ using triangularly truncated spherical harmonics. Abusing notation by switching temporarily from Cartesian coordinates x, y to spherical coordinates θ, φ, we have

$$\chi(\theta, \varphi, t) = \sum_{n=0}^{N} \sum_{m=-n}^{n} \hat{\chi}_n^m(t) Y_n^m(\theta, \varphi). \tag{5}$$

Here m and n denote nondimensional zonal and total wavenumbers, respectively; N is a cut-off wavenumber; Y_n^m are L^2-orthogonal basis functions on the sphere; and $\hat{\chi}_n^m(t)$ are spherical harmonic coefficients each of which is an Ornstein-Uhlenbeck process. At the discrete level, the coefficients $\hat{\chi}_n^m(t)$ are independent Gaussian autoregressive processes of order one (AR1):

$$\hat{\chi}_n^m(t + \Delta t) = \phi \hat{\chi}_n^m(t) + g_n \sqrt{1 - \phi^2} \epsilon_n^m(t) \tag{6}$$

where $\phi = e^{-\Delta t/\tau}$, Δt is the time step, τ is the decorrelation time (here 6 hr), and $\epsilon_n^m(t)$ are independent and identically distributed standard Gaussians. The mean of each coefficient is zero. The coefficients are initialized independently of $\epsilon_n^m(t)$ with variance g_n^2, which ensures that their variance remains g_n^2 for all time. The structure of the variances g_n^2 controls the spatial structure of the velocity increments, as described below. The random field is evaluated on a Gaussian grid and then bilinearly interpolated to the OGCM grid. Future work may replace the AR1 process, which is a discretization of a continuous but non-differentiable Ornstein-Uhlenbeck process by an autoregressive model that discretizes a stochastic process with one or more continuous derivatives, following Grooms (2016).

2.2.1. Kinetic Energy Forcing Spectrum

To obtain the one-dimensional kinetic energy spectrum, first apply the negative Laplacian to Equation 5, which produces a factor of $-n(n + 1)/R^2$ where R is the radius of the Earth. Next multiply by the sum Equation 5 and take the expected value; the fact that the coefficients $\hat{\chi}_n^m$ are all independent leads to an expression of the form

$$\mathbb{E}\left[\chi\left(-\nabla^2\chi\right)\right] = \frac{1}{R^2} \sum_{n=0}^{N} \sum_{m=-n}^{n} n(n+1) \mathrm{Var}\left[\hat{\chi}_n^m(t)\right] \left|Y_n^m(\theta, \varphi)\right|^2. \tag{7}$$

Here and throughout, the ∇ notation indicates derivatives taken with respect to the horizontal coordinates only. Next integrate over the surface of the sphere, using integration by parts on the left and unit L^2 norm of the spherical harmonics on the right, which produces

$$\mathbb{E}\left[|\nabla\chi|^2\right] = \frac{1}{R^2}\sum_{n=0}^{N}\sum_{m=-n}^{n} n(n+1)\mathrm{Var}\left[\hat{\chi}_n^m(t)\right]. \tag{8}$$

The spatial structure of the noise is set by the variances g_n^2 of the coefficients $\hat{\chi}_n^m(t)$.

We can interpret the velocity increments as resulting from the divergence of stresses resulting from unresolved mesoscales. A simple *prima facie* model is that the subgrid stresses are uncorrelated on the scales resolved by the OGCM, so that their two-dimensional spectrum is flat (Schumann, 1995). The one-dimensional spectrum of the stresses (averaged over zonal wavenumbers m in this case) is then proportional to the total wavenumber n. Since the velocity increment spectrum is proportional to the spectrum of the divergence of the subgrid stresses, the velocity increment spectrum would then be proportional to n^3. Practically speaking, it is inadvisable to backscatter directly into the model's dissipation range, so the spectrum should be modified toward zero at the smallest scales resolvable on the grid (cf. Grooms et al., 2015b).

With this in mind, the variances of the coefficients $\hat{\chi}_n^m(t)$ are here chosen to be a Gaussian function of total wavenumber n only,

$$g_n^2 = \mathrm{Var}\left[\hat{\chi}_n^m(t)\right] \propto e^{-\frac{L_{\mathrm{stoch}}^2}{16R^2}n(n+1)}. \tag{9}$$

The proportionality constant in Equation 9 is independent of n, m, and t, and serves to normalize the random field so that, if $\phi = M = 1$ and if A were constant, the expected value of the local kinetic energy density of the velocity increments would be equal to A^2 uniformly in time and space (cf. Equation 5 in Berner et al., 2009). Inserting Equation 9 into Equation 8 and noting that the summand is independent of m yields the following expression for the kinetic energy spectrum of the increments

$$\mathbb{E}\left[|\nabla\chi|^2\right] \propto \sum_{n=0}^{N} n(n+1)(2n+1)e^{-\frac{L_{\mathrm{stoch}}^2}{16R^2}n(n+1)}. \tag{10}$$

The length scale L_{stoch} in Equation 9 controls the wavenumber of the peak of the kinetic energy injection spectrum. Specifically, for $L_{\mathrm{stoch}} \ll R$, the peak of the kinetic energy injection spectrum is at dimensional wavelength

$$\lambda_{\max} \sim \frac{\pi}{\sqrt{6}} L_{\mathrm{stoch}}. \tag{11}$$

The KE forcing spectrum is plotted in Figure 1 for three different values of $L_{\mathrm{stoch}} = 120$, 240, and 480 km, as used in the simulations described below. The truncation level N in the plot is set to 258, as used in the simulations, which corresponds to a wavelength of 156 km. Consistent with the heuristic argument above, the KE forcing spectrum used here is proportional to n^3 over a wide range of scales, rising to a peak as indicated above, after which it drops rapidly at smaller scales.

Naturally the length scale of the forcing L_{stoch} should be set to a value larger than the grid scale of the model. In fact, since L_{stoch} is a wavelength, it should be set larger than the smallest wavelength locally representable on the grid, which is twice the grid scale. Furthermore, since the dynamics of length scales close to the grid scale are not well-resolved and are typically dominated by explicit and numerical dissipation, one might want to avoid forcing directly in the model's dissipation range by letting L_{stoch} be two or three times larger than the minimum grid wavelength, that is, one might set $L_{\mathrm{stoch}} \geq 4\Delta x$ where Δx is the model grid spacing. On the other hand, one cannot set L_{stoch} too large because, as noted in the discussion of Equation 3, there needs to be a scale separation between χ and A and ϕ.

2.3. Amplitude

Provided that A and ϕ vary slowly compared to χ in the lateral directions, and away from boundaries, the mean kinetic energy of the velocity increments is $A^2\phi^2$. Ignoring any correlations between the velocity at the end of a

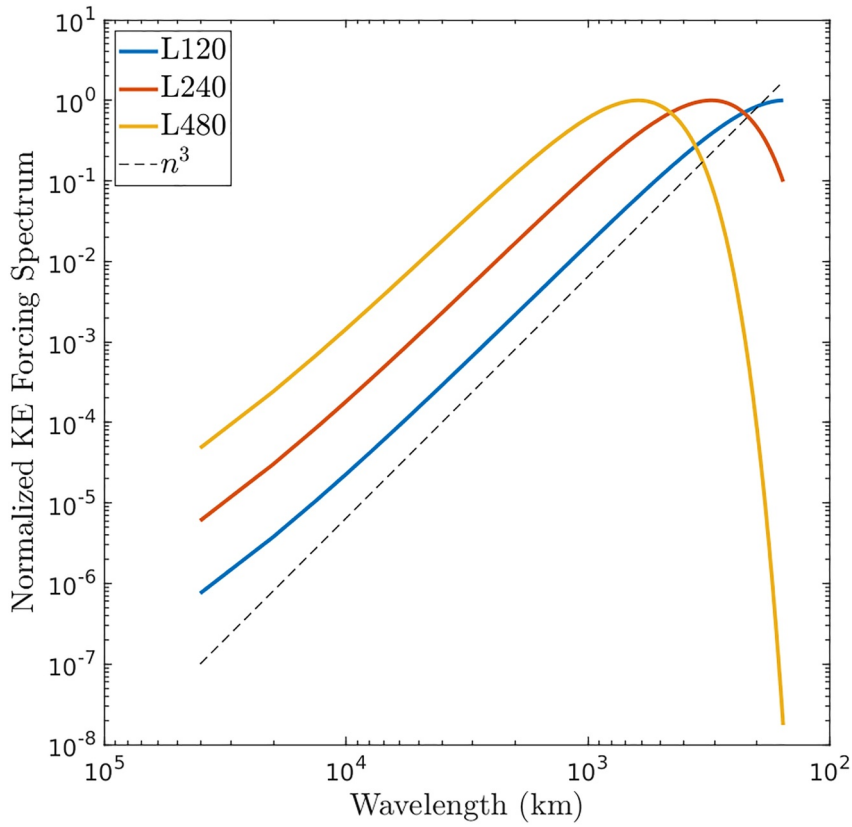

Figure 1. The kinetic energy spectra that the velocity increments would have if both A and ϕ were constant, for three different values $L_{\text{stoch}} = 120$, 240, and 480 km. The spectra are normalized to reach a unit maximum, and are therefore nondimensional. The dashed line is proportional to n^3. The spectra are truncated at $N = 258$, as used in the simulations, which corresponds to a wavelength of 156 km.

time step and the increment added after the end of the time step, the mean rate at which the stochastic increments increase the kinetic energy of the flow is

$$\frac{A^2\phi^2}{\Delta t} \tag{12}$$

where Δt is the length of the time step. The error incurred by ignoring correlations between the velocity at the end of a time step and the increment added after the end of the time step is addressed in Appendix A. This approximation—ignoring correlations between the velocity and the velocity increments—is supported by the use of a very short decorrelation time τ for the increments, here τ is 6 hours. The distribution of the increments across depth is discussed in the next subsection; in this subsection we consider the depth-averaged amplitude, and assume that the depth average of ϕ^2 is one

$$\frac{1}{H}\int_{-H}^{0}\phi^2(z)\mathrm{d}z = 1. \tag{13}$$

We want the depth-averaged mean rate of kinetic energy injection by the stochastic increments to be proportional to the depth-averaged rate of potential energy loss associated with the GM parameterization. Denote this latter rate by W_{GM}, and let it be called the "GM work rate" for brevity. Recall that we are normalizing it to be the rate of potential energy loss per unit mass consistent with our convention for kinetic energy. The details of this loss rate are strongly dependent on the details of the GM parameterization being used—the magnitude of the GM coefficient κ, its vertical structure, the vertical coordinate being used by the model, etc—so we refrain from providing

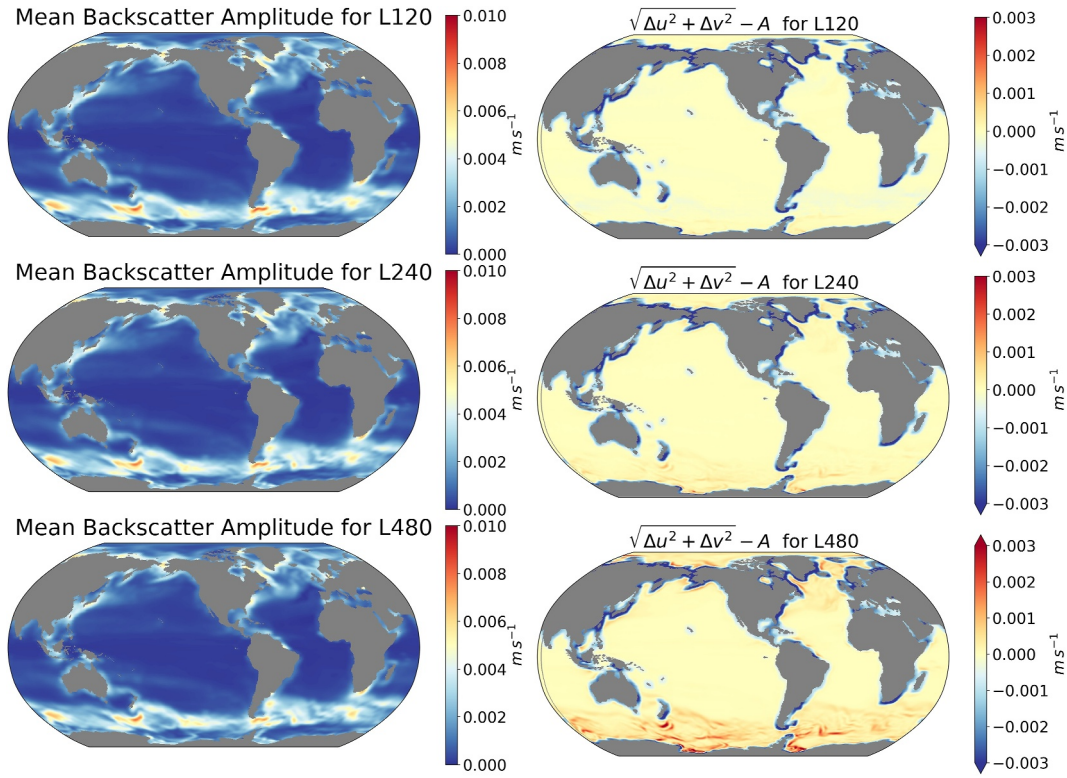

Figure 2. Left column: Backscatter amplitude A. Right column: Difference between the diagnosed amplitude of the stochastic velocity increments $\sqrt{\Delta u^2 + \Delta v^2}$ and the backscatter amplitude A. L120, L240, and L480 results are shown in the upper, middle, and lower panels, respectively. (m s^{-1}).

a formula for W_{GM}. Assuming instead that W_{GM} is already available within the model, we achieve the desired relationship between the GM work rate and stochastic backscatter by setting

$$A = [c\Delta t W_{\mathrm{GM}}]^{1/2} \tag{14}$$

where $c \in [0, 1]$ determines the fraction of the GM work that is backscattered as kinetic energy.

Recall, though, that the mean rate of kinetic energy injection by the stochastic increments is approximately equal to $A^2/\Delta t$ only if A and ϕ vary slowly compared to χ in the lateral directions. The GM work rate can vary on a scale that is not much larger than the grid scale of the model, which means that A can also vary on short length scales. This does not leave much room for χ to vary on a length scale much shorter than A, yet still be resolvable on the grid. To alleviate this problem we apply a spatial filter to W_{GM} before using it to determine the amplitude A:

$$A = \left[c\Delta t \bar{W}_{\mathrm{GM}}\right]^{1/2} \tag{15}$$

The overbar denotes $N_{\mathrm{smooth}} = 8$ passes of a nine-point moving average filter whose weights are proportional to the grid cell areas.

The number of smoothing passes is tunable. Though computationally inexpensive, smoothing can incur high communication costs in some settings. Nevertheless, the number of smoothing passes should not be set too low: if the amplitude A varies on a length scale that is not much larger than the length scale of χ, then not only will the amplitude of the backscatter not be proportional to A, but also the length scale at which the energy is injected will not be primarily controlled by the scale L_{stoch} of χ.

The left column of Figure 2 shows the amplitude A from three simulations using $L_{\mathrm{stoch}} = 120$, 240, and 480 km. (The experimental configuration is described in more detail in Section 3.) Backscatter is active wherever the GM

parameterization removes potential energy from the resolved flow: primarily in the Southern Ocean, but also in boundary currents and their extensions in the northern hemisphere. The right column shows the difference between the mean amplitude of the stochastic velocity increments diagnosed online during the model run and the intended amplitude A. These differences arise because of discretization errors, because of tapering, and because the amplitude A and vertical structure ϕ are not exactly independent of the horizontal coordinates. The first thing that stands out are the regions near the coasts where blue colors indicate that the design amplitude is larger than the actual amplitude. These blue regions show where the taper function M_{taper} is active. There is not a blue halo around the entire lateral boundary because backscatter is not active everywhere.

The upper right panel shows that when $L_{\text{stoch}} = 120$ km the actual amplitude of the stochastic increments matches the intended amplitude A well everywhere except near boundaries. At $L_{\text{stoch}} = 240$ km some discrepancies appear in the Southern Ocean where the actual backscatter is larger than designed. At $L_{\text{stoch}} = 480$ km the actual backscatter is larger than designed over much of the Southern Ocean as well as in the North Atlantic and parts of the Arctic Ocean. This illustrates that the design and actual backscatter rates can be different when the length scale of the random pattern encroaches on the length scale of the amplitude A.

We suggest the following conservative heuristic for choosing N_{smooth}. Let Δx be the smallest grid size in the region of the model where the stochastic parameterization is active. The smoother attenuates wavenumber k in W_{GM} by a factor of $[(1 + 2\cos(k\Delta x))/3]^{N_{\text{smooth}}}$. We want there to be very little energy in $\bar{W}_{\text{GM}}$ at the length scales where the stochastic forcing is active, so we set $k = 2\pi/\lambda_{\max} = 2\sqrt{6}/L_{\text{stoch}}$ and choose N_{smooth} so that the attenuation factor is appropriately small. For $L_{\text{stoch}} = 240$ km and $\Delta x = 40$ km (a value relevant at 60°S in our model) the attenuation factor is 0.15 with $N_{\text{smooth}} = 8$. For $L_{\text{stoch}} = 480$ km and $\Delta x = 40$ km the attenuation factor is 0.64 with $N_{\text{smooth}} = 8$.

2.4. Vertical Structure

The scales resolved by coarse OGCMs are close to quasigeostrophic or planetary-geostrophic balance (Grooms et al., 2011, 2012). The stochastic velocity increments added to the background velocity are not balanced: though laterally incompressible, any vertical shear is not in thermal-wind balance with a corresponding lateral buoyancy gradient. Adding imbalanced velocity increments leads to a geostrophic adjustment process where inertio-gravity waves are radiated, and where some of the increments' kinetic energy is converted to potential energy. Since the resolved flow is mostly balanced, with little wave energy, we would like to avoid having the stochastic increments generate significant internal wave energy.

One way to avoid this would be to let the velocity increments be depth-independent, that is, barotropic. Barotropic increments would not radiate internal waves, nor would there be any conversion of kinetic to potential energy during the adjustment process. A significant downside of barotropic increments is that they would induce flow near the bottom, where flows are typically weak, and would radiate waves through topographic interactions. We therefore seek a vertical structure with no flow at the bottom, which also minimizes the radiation of internal waves.

Consider a local patch of ocean where

$$N^2(z) = -\frac{g\partial_z \rho}{\rho} \tag{16}$$

is approximately independent of time and horizontal location (where g is the gravitational acceleration and ρ is potential density), and assume that the amplitude A and vertical structure ϕ of the velocity increment are also approximately constant over this patch of ocean. According to the classical theory of geostrophic adjustment, the potential vorticity of the adjusted state is the same as that of the initial condition (Blumen, 1972), where the initial condition in this case is the velocity increment. The quasigeostrophic potential vorticity of the increment is simply its vorticity

$$q = A\phi(z)\nabla^2\chi \tag{17}$$

where $\nabla^2 = \partial_x^2 + \partial_y^2$ and both A and ϕ are assumed to vary only slowly in the lateral directions. The adjusted state will have a quasigeostrophic streamfunction Ψ that is related to the potential vorticity q by

$$\nabla^2\Psi + \partial_z\left(\frac{f^2}{N^2}\partial_z\Psi\right) = q \tag{18}$$

where f is the local Coriolis parameter. Since $q = 0$ at the bottom of the ocean, it is natural to expand both it and Ψ with respect to a basis of eigenfunctions $p_n(z)$ satisfying

$$\partial_z\left(\frac{f^2}{N^2}\partial_z p_n\right) = -k_n^2 p_n \text{ for } z \in (-H, 0) \tag{19a}$$

$$p_n(-H) = 0, \qquad \partial_z p_n\big|_{z=0} = 0. \tag{19b}$$

The eigenfunctions p_n are known as surface modes, and the eigenvalues $-k_n^2$ related to so-called surface deformation radii λ_n by $\lambda_n = 1/k_n$ (de La Lama et al., 2016; Lacasce, 2017). The use of the term "mode" here should not be misconstrued to suggest that these vertical structures are necessarily related to normal modes of the linearized governing equations (for a discussion of quasigeostrophic normal modes see Yassin & Griffies, 2022); rather, they are simply a convenient basis. By similar arguments to those advanced by Rocha et al. (2016, Appendix A) for the classical baroclinic mode basis, an expansion in surface modes can be shown to converge absolutely and uniformly for any continuously differentiable function on $z \in [-H, 0]$ with zero bottom boundary condition.

The expansions of q and Ψ are

$$q = \sum_{n=1}^{\infty} \hat{q}_n(x,y)p_n(z), \text{ and } \Psi = \sum_{n=1}^{\infty} \hat{\Psi}_n(x,y)p_n(z). \tag{20}$$

The vertical structure of q is determined entirely by the $\phi(z)$, so we have

$$\phi(z) = \sum_{n=1}^{\infty} \hat{\phi}_n p_n(z), \text{ and} \tag{21}$$

$$\hat{q}_n = A\hat{\phi}_n\nabla^2\chi. \tag{22}$$

The expansion coefficients are related by

$$\nabla^2\hat{\Psi}_n - k_n^2\hat{\Psi}_n = \hat{q}_n = A\hat{\phi}_n\nabla^2\chi. \tag{23}$$

Assuming that the eigenfunctions are normalized so that

$$\frac{1}{H}\int_{-H}^{0} p_n(z)^2 \mathrm{d}z = 1, \tag{24}$$

the depth-averaged kinetic energy of the state after geostrophic adjustment is

$$\frac{1}{2}\sum_{n=1}^{\infty} |\nabla\hat{\Psi}_n|^2 \tag{25}$$

and the depth-averaged quasigeostrophic available potential energy of the adjusted state is

$$\frac{1}{2}\sum_{n=1}^{\infty} k_n^2 \hat{\Psi}_n^2. \tag{26}$$

To assess how much energy will be radiated away as internal waves requires one more assumption, that

$$\nabla^2 \chi \approx -\frac{4\pi^2}{L_{\text{stoch}}^2}\chi, \tag{27}$$

which is reasonably accurate given that the kinetic energy forcing spectrum from Section 2.2 is peaked near wavenumber $2\pi L_{\text{stoch}}^{-1}$. This assumption implies that

$$\hat{\Psi}_n = \frac{4\pi^2 A}{4\pi^2 + L_{\text{stoch}}^2 k_n^2}\chi. \tag{28}$$

The depth-averaged kinetic energy of the adjusted state is therefore

$$\frac{2\pi^2}{L_{\text{stoch}}^2}\left(\frac{4\pi^2 A}{4\pi^2 + L_{\text{stoch}}^2 k_n^2}\right)^2 \chi^2. \tag{29}$$

For the sake of argument, suppose that we choose to let $\phi(z) = p_n(z)$ for some mode number n. The depth-averaged kinetic energy in the initial state, that is, the velocity increment, is

$$\frac{2\pi^2 A^2}{L_{\text{stoch}}^2}\chi^2. \tag{30}$$

The ratio of the depth-averaged total energy in the adjusted state to the depth-averaged kinetic energy in the velocity increment is

$$\frac{\text{Adjusted Energy}}{\text{Increment KE}} = \left(\frac{4\pi^2}{4\pi^2 + L_{\text{stoch}}^2 k_n^2}\right)^2. \tag{31}$$

Since k_n increases with n, we can see that higher mode structures end up radiating more of their energy away as waves, so to minimize the radiation of wave energy we choose

$$\phi(z) = p_1(z). \tag{32}$$

The surface deformation radius $\lambda_1 = 1/k_1$ is similar to the baroclinic deformation radius over much of the globe (LaCasce & Groeskamp, 2020, Figure 8). Outside the tropics it is smaller than the typical grid scale of a coarse OGCM, and given the requirement from Section 2.2 that L_{stoch} be at least a factor of 4 larger than the grid scale, the analysis predicts that a significant amount of the kinetic energy from the stochastic increments to propagate as large-scale internal waves. In contrast, a parameterization that backscatters potential energy, like that of Grooms (2016), would generate less internal wave energy, but would still induce variability in the balanced flow. It bears noting that this analysis is based on linearization around a state of rest with no lateral density gradients, assumptions that are not met in the global ocean, so the predictions about the amount of energy radiated as internal waves are at best qualitatively accurate.

3. Experimental Configuration

3.1. Model Configuration

The stochastic GM + E backscatter parameterization described in Section 2 has been implemented in the Modular Ocean Model version 6 (MOM6) ocean model (Adcroft et al., 2019). Its effects are explored here in the CESM2

framework (Danabasoglu et al., 2020) with active ocean and sea-ice components. The horizontal grid has a nominal 2/3° spacing with meridional refinement to 1/4° in an equatorial band. At 66°S the grid size is approximately 30 km. It rises rapidly toward the equator to approximately 40 km at 57°S and 57 km at 40°S. At 35°S the grid size is approximately 60 km. The vertical coordinate is z^*, with a vertical grid of 65 levels with thicknesses from 2.5 m at the surface to 250 m depth. Except as noted below, the configuration follows that of Marques et al. (2023).

Unlike Marques et al. (2023) we use zero Laplacian viscosity, and we use a biharmonic "2D-Leith" viscosity following Grooms (2023), but without the backscatter scheme developed by Grooms (2023). The nondimensional Leith coefficient Υ is set to $8^{1/6}$. Mixed-layer restratification by submesoscale baroclinic instability is parameterized following Bodner et al. (2023).

The Redi tracer diffusivity is parameterized using the approach of Marshall et al. (2012):

$$\kappa_{\mathrm{KHTR}} = \alpha e \frac{1}{H}\int_{-H}^{0} \frac{N(z)}{M^2(z)}\mathrm{d}z \tag{33}$$

where $\alpha = 0.09$, e is the unresolved mesoscale eddy kinetic energy (detailed below), N^2 is defined by Equation 16, and

$$M^2(z) = -\frac{g|\nabla\rho|}{\rho}. \tag{34}$$

The GM and Redi coefficients match at the surface, but the GM coefficient decays with depth following the profile of the first surface mode: the GM coefficient is $\kappa_{\mathrm{KHTH}}(z) = \big(p_1(z)/p_1(0)\big)\kappa_{\mathrm{KHTR}}$.

The unresolved mesoscale eddy kinetic energy e is parameterized using the prognostic formulation of Jansen et al. (2019), their Equation 12. The lateral diffusivity of e is set to 75% of the rate for tracers κ_{KHTR}, following the findings of Grooms (2017). Where Marques et al. (2023) did not use the rate at which the biharmonic viscosity removes resolved kinetic energy as a source term for e, we use 30% of this rate as a source for e. The coefficient c_b from Equation 12 of Jansen, Adcroft, et al. (2015) that appears in the formulation of the rate of loss of e to bottom friction is increased from 25 to 100, which has the effect of reducing the amount of e lost to bottom friction.

The physics and other settings used in the MOM6 configuration of CESM are constantly being improved. This description here only applies to the specific version of MOM6 that was used for the experiments in this paper.

3.2. Experimental Design

The simulations are forced using repeated cycles of the JRA55-do v1.4 data set (Tsujino et al., 2018). One forcing cycle covers the years 1958 through 2018 for a total of 61 years. We spun up a control experiment without stochastic forcing for one full JRA cycle of 61 years, initializing from rest and using temperature and salinity fields from the 2018 World Ocean Atlas. Five stochastic experiments were initialized from the end of the 61 $^{\mathrm{st}}$ year of the control experiment. The control experiment and these five stochastic experiments were then run for another full JRA cycle, that is, 61 more years. Unless otherwise stated, the results presented in the next section have been averaged over the last 50 years of the simulations.

The primary tunable parameter in the stochastic GM + E backscatter scheme is the fraction c of the GM work rate that is backscattered as kinetic energy. Lacking a flow-aware and scale-aware theory for c, we resort to sensitivity testing by considering three values of c: 0.25, 0.5, and 0.75. Varying this parameter in this model is complicated by the use of the prognostic equation for subgrid-scale eddy kinetic energy: to maintain energetic consistency, the fraction of the GM work that appears as a source term in the e budget is set to $1 - c$.

Figure 3 shows the change in the time-mean mesoscale eddy kinetic energy e between the run with $c = 0.25$ (labeled c25) and a run with $c = 0.5$ (upper left) and between the run with $c = 0.75$ (labeled c75) and a run with $c = 0.5$ (upper right); the run with $c = 0.5$ uses $L_{\mathrm{stoch}} = 240$ km and is thus labeled L240. The amount of parameterized mesoscale eddy kinetic energy e increases slightly with increasing c. With lower values of c the amount of GM work that appears as a source term in the e budget increases, so one might expect e to be larger at

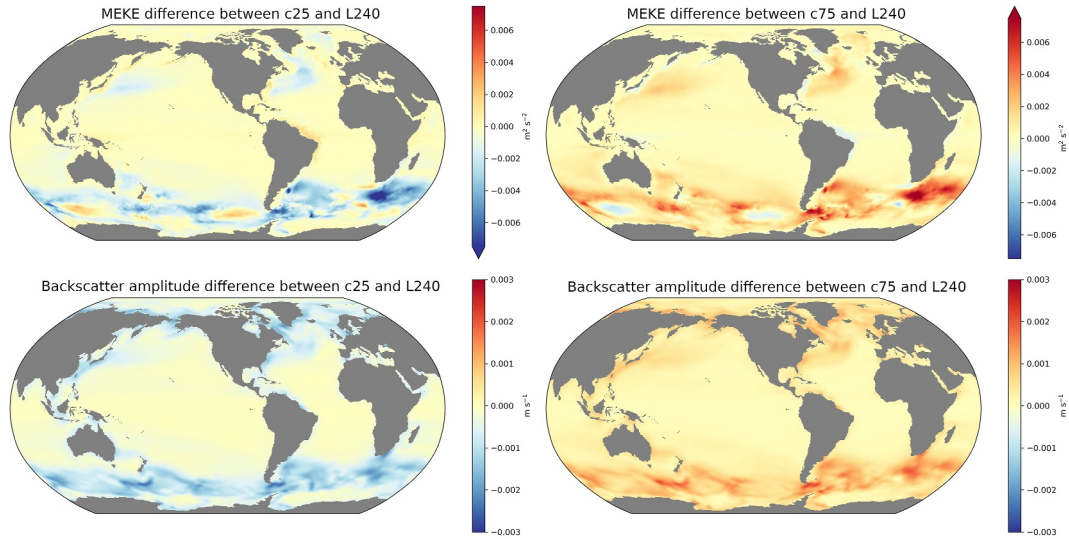

Figure 3. Top: Differences in time-mean MEKE e ($m^2\ s^{-2}$) for runs with $L_{stoch} = 240$ km: $c = 0.25$ minus $c = 0.5$ (left); $c = 0.75$ minus $c = 0.5$ (right). Bottom: Differences in time-mean amplitude A ($m\ s^{-1}$) for runs with $L_{stoch} = 240$ km: $c = 0.25$ minus $c = 0.5$ (left); $c = 0.75$ minus $c = 0.5$ (right).

lower c values. Indeed, at $c = 0.5$ the mean rate at which GM removes energy from the resolved flow is 0.0011 W m^{-2}; at $c = 0.25$ this value decreases by 6.5% and at $c = 0.75$ this value increases by 6.5%. When accounting for the factor of $1 - c$ that multiplies the GM work rate in the budget for e, the amount by which GM work forces e decreases as c increases. This is offset by the fact that 30% of the rate at which the biharmonic viscosity removes resolved kinetic energy is added as a source term for e. In the L240 simulation the biharmonic lateral viscosity removes resolved kinetic energy at an average rate of 0.0019 W m^{-2}; 30% of this is added as a forcing to e. At $c = 0.25$ there is less backscatter and therefore also less kinetic energy dissipation, so the biharmonic work rate decreases by 17%; at $c = 0.75$ there is more backscatter, so the biharmonic work rate increases by 19%. This is enough to offset the reduced input to e from GM work, with the effect that e increases slightly with increasing c. There are local deviations from this behavior in the Southern Ocean. We presume that increasing the backscatter fraction from 0.25 through 0.75 leads to increased variability in the resolved currents that advect e, which spreads it out more and accounts for the local changes in e in the south Pacific and Indian oceans.

The lower panels of Figure 3 show the changes in backscatter amplitude A as c changes. Despite the changes in e shown in the upper panels, the actual backscatter rate changes as expected with c: decreasing c from 0.5 to 0.25 leads to a decrease in A (lower left), while increasing c from 0.5 to 0.75 leads to an increase in A (lower right).

The second important tunable parameter in the scheme is the length scale L_{stoch} of the stochastic forcing. As described in Section 2.2, this value should be sufficiently large compared to the grid scale, yet not too large. Figure 2 shows that the backscatter is strongest in the Southern Ocean, as well as at mid and high latitudes in the northern hemisphere. At these latitudes, the grid spacing lies in the range of approximately 40–60 km. We therefore test three length scales for the backscatter: $L_{stoch} = 120$, 240, and 480 km. The smallest is near the minimum recommendation $L_{stoch} \geq 4\Delta x$ in mid and high latitudes, while the largest is encroaching on the scale over which the backscatter amplitude varies. These three simulations are denoted L120, L240, and L480, and all use $c = 0.5$, that is, they backscatter 50% of the GM work rate into kinetic energy. The simulations using $c = 0.25$ and $c = 0.75$ both use $L_{stoch} = 240$ km and are denoted c25 and c75, respectively. The spherical harmonic truncation level N is set to 258, which corresponds to a wavelength of 156 km, which is close to the grid wavelength of 120 km in midlatitudes.

4. Results

We begin this section by showing how the parameterization affects the mean state and bulk diagnostics. Since the configuration of CESM-MOM6 used here is merely a snapshot within an ongoing development process where biases in the mean state are continually changing, we do not show biases with respect to observations; we instead

only show how the parameterization changes the mean state compared to the control run. We then move on to showing how the parameterization affects the model variability. In the context of variability, we compare the control and stochastic simulations to observational products to demonstrate that the parameterization improves variability. We focus on results at $c = 0.5$; where results at $c = 0.25$ and $c = 0.75$ are not shown, the conclusions are qualitatively similar, but different in amplitude.

The stochastic parameterization adds computational cost, primarily associated with evolving the stochastic spherical harmonic coefficients, and evaluating the random pattern on the model grid. The control simulation achieves a throughput of 25.5 simulated years per day, while the L240 simulation achieves only 22 simulated years per day. All the stochastic similations have similar throughput since they all share the same number of smoothing passes $N_{\text{smooth}} = 8$ and spherical harmonic truncation level $N = 258$ in Equation 5. The addition of stochastic backscatter thus reduces throughput by about 14%.

4.1. Mean State and Bulk Diagnostics

The upper panel of Figure 4 shows the global kinetic energy over time. The addition of stochastic backscatter at the beginning of year 62 rapidly increases the kinetic energy by about 3 PJ (on the order of 15%) for all values of L_{stoch} at $c = 0.5$. The increase is smaller for $c = 0.25$ and larger for $c = 0.75$.

The middle panel of Figure 4 shows time series of the volume transport through Drake Passage. The addition of stochastic backscatter reduces the total transport by about 10 Sv for $c = 0.5$ and $c = 0.75$, with a slightly smaller reduction for $c = 0.25$ and minimal sensitivity to L_{stoch}. Drake Passage transport can take several JRA55 cycles to equilibrate, so these results may not be representative of the equilibrated state of the models. Drake Passage transport could be adjusted by tuning of the α parameter that controls the strength of the GM coefficient.

The lower panel of Figure 4 shows the change in global mean potential temperature over time. The drift is small—on the order of $1/8$°C over the first JRA cycle—and the addition of stochastic backscatter tends to reduce the drift. The effect is smaller with weaker backscatter $c = 0.25$ and increases as the backscatter coefficient increases to $c = 0.5$ and 0.75. Since the forcing comes from a reanalysis product that includes a secular drift in temperature, one does not expect the global mean ocean potential temperature to remain constant over the forcing cycle.

Figure 5 shows the global temperature drift as a function of depth for the control run (left) and for the L240 run (right). The first 61 years are the same in both panels, and indicate an increase in temperature in the upper kilometer of the ocean. This drift continues during the second forcing cycle in the control run, but partially reverses in the L240 run. Notably, the impact of the stochastic forcing on the drift is opposite to the effect of diapycnal mixing, including spurious diapycnal mixing associated with discretization errors, which mixes warm water downwards. Although all simulations are warming at the end of the second forcing cycle, both Figures 4 and 5 show that the effect of our backscatter on ocean heat uptake is the opposite to the effect of the stochastic backscatter scheme of O'Kane et al. (2023), who saw an increase in ocean heat uptake.

The upper left panel of Figure 6 shows the difference between the mean SST in the L240 and control runs. In the northern Pacific the stochastic parameterization reduces the mean SST gradient across the Kuroshio extension. In the northern Atlantic the center of the subpolar gyre is warmed while there is both warming and cooling in the vicinity of the North Atlantic Current. In the Southern Ocean the SST gradient across the subtropical front is reduced. These SST changes are all consistent with increased heat transport across fronts. The warming in the center of the north Atlantic subpolar gyre opposes a persistent bias common to many OGCMs (Bryan et al., 2007; Moreno-Chamarro et al., 2022; Smith et al., 2000).

The upper right panel of Figure 6 shows the difference between the mean SSH in the L240 and control runs. Here and throughout, SSH does not include thermosteric effects. In the northern Atlantic and Pacific the gradient across the SSH front between the subtropical and subpolar gyres is reduced slightly. In the Southern Ocean the SSH gradient across the Antarctic Circumpolar Current is also somewhat reduced, which is consistent with the reduction in Drake Passage transport shown in Figure 4. The changes in mean SST and SSH in the L120 and L480 runs are qualitatively consistent with the changes shown for L240 in Figure 6 (not shown).

The lower panel of Figure 6 shows the difference between the winter mean mixed layer depths in the L240 and control runs, where mixed layer depth is defined by the Sigma T criterion with $\Delta\rho = 0.03\ \text{kg m}^{-3}$. In the Southern Ocean the addition of stochastic backscatter leads to a southward shift of the deep mixing band in the Indian and

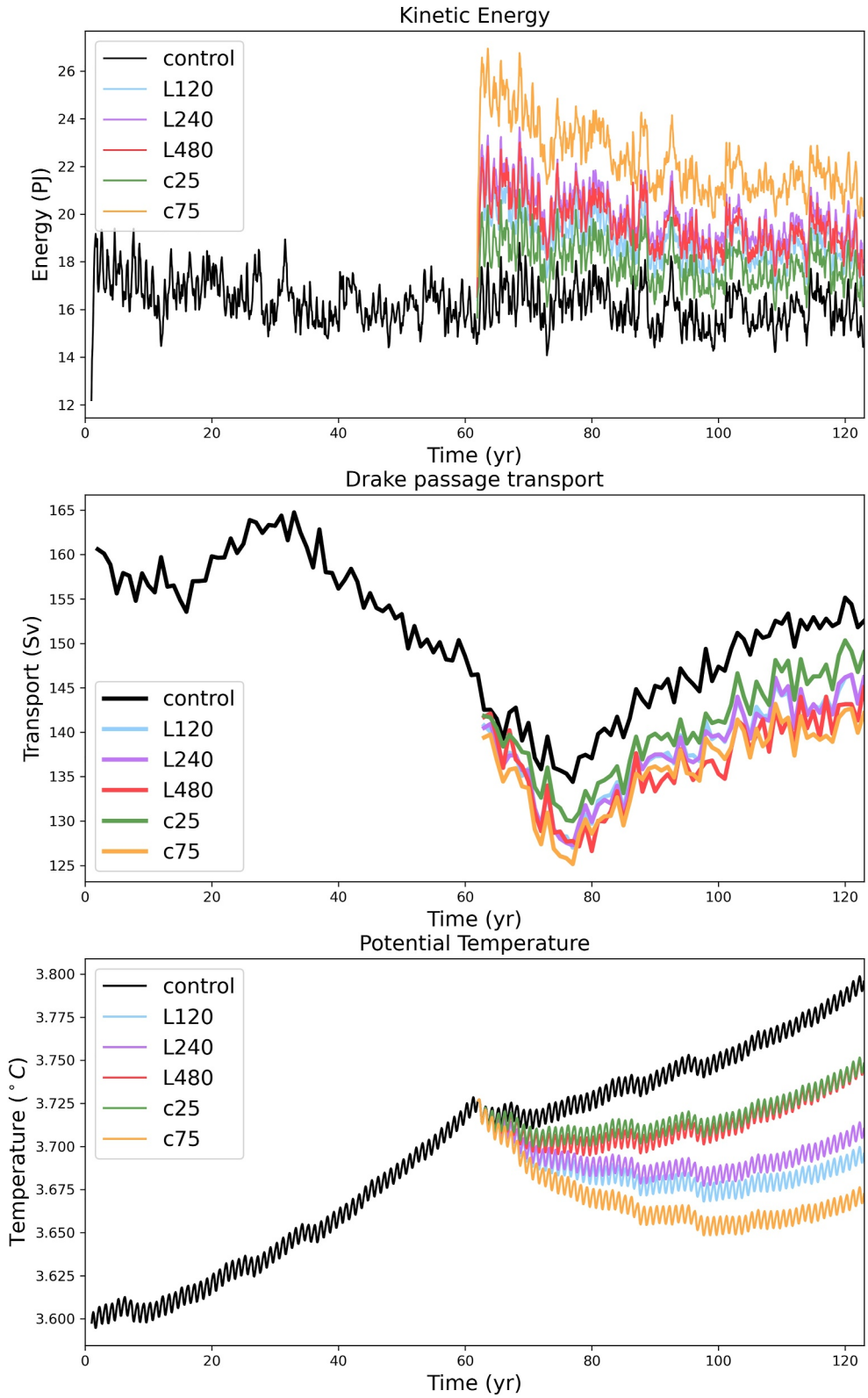

Figure 4. Top: Time series of total kinetic energy (PJ). Middle: Time series of volume transport through Drake Passage (Sv). Bottom: Time series of volume-mean potential temperature (°C). The JRA atmospheric forcing cycle repeats starting in year 61, which is also when the stochastic simulations branch from the control run.

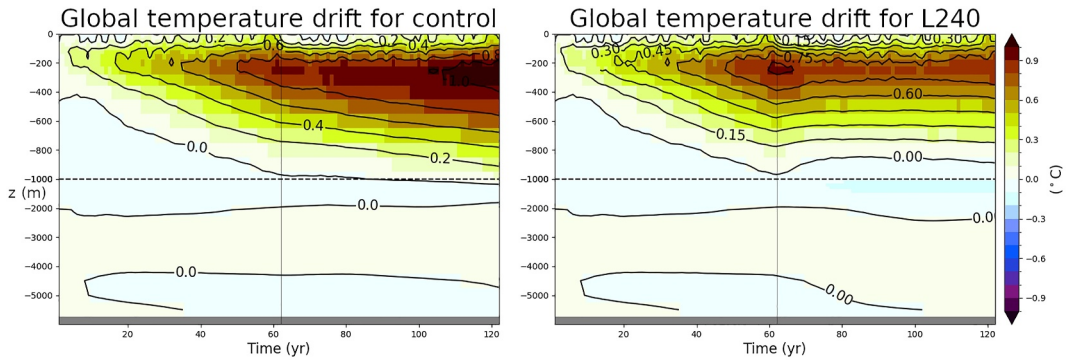

Figure 5. Global mean potential temperature as a function of depth and time for the control run (left) and L240 (right). The two panels are the same for the first 61-year forcing cycle, the end of which is indicated by a vertical line. The plots only differ in the second forcing cycle, that is, to the right of the vertical line.

Pacific sectors. This deepening is consistent with the change in SST in the same region shown in the upper left panel. It also leads to a deepening of the mixed layers in the center of the Labrador sea; other differences are not significant.

Figure 7 summarizes the changes in sea ice area. The top left panel shows the northern hemisphere total sea ice area in March for each year of the simulation. The stochastic backscatter has negligible impact on total sea ice area in the northern hemisphere. The top right panel shows the total sea ice area in the southern hemisphere in September for each year of the simulation. Southern hemisphere sea ice area is reduced by the stochastic parameterization by one to one-half million square kilometers. Observational estimates place the total sea ice area in the southern hemisphere at 13 to 15 million square kilometers, and both simulations are near the CMIP6 multi-model mean (Roach et al., 2020). The lower panels of Figure 7 show the September mean sea ice concentration for the control simulation (left) and the change in the L240 simulation (right). Sea ice concentration in L240 is reduced almost uniformly around its outer edge, which is consistent with the increase in SST shown in Figure 6.

4.2. Variability

Figure 8 shows daily mean surface speed on July 1 of the last year of the simulations for the control run and the three stochastic runs with $c = 0.5$. The figure shows a subset of the South Atlantic, Southern Ocean, and Weddell

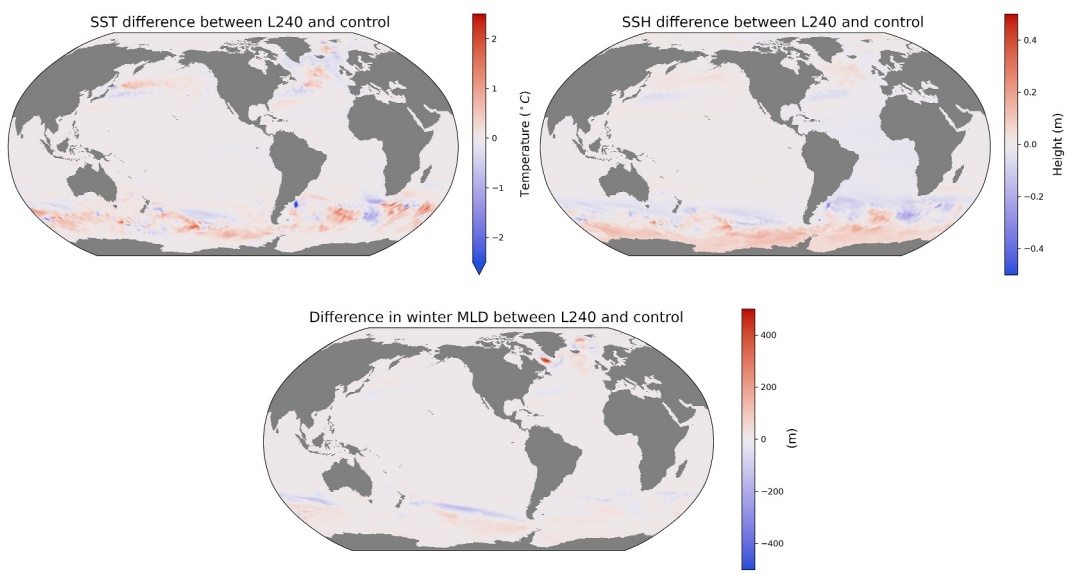

Figure 6. Upper left: Mean SST in L240 minus mean SST in the control run (°C). Upper right: Mean SSH in L240 minus mean SSH in the control run (m). Bottom: Winter mean mixed layer depth, L240 minus control (m).

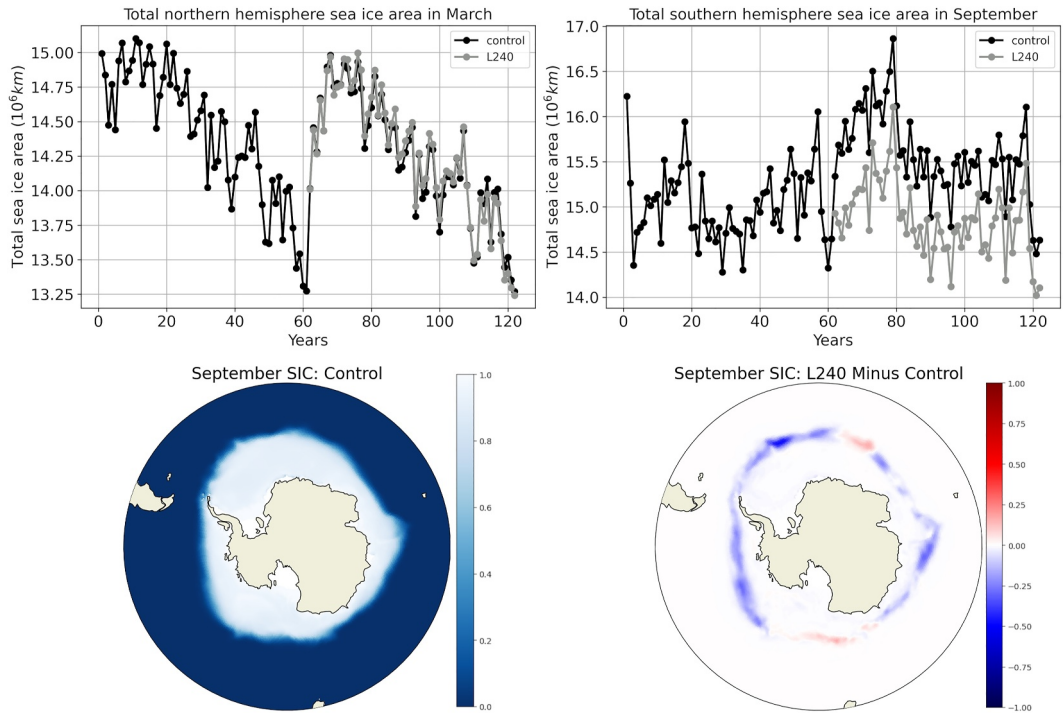

Figure 7. Top left: March-mean total sea ice area in the northern hemisphere for the control run (black) and L240 (gray). Top right: September-mean total sea ice area in the southern hemisphere for the control run (black) and L240 (gray). Lower left: September-mean sea ice concentration for the control run (nondimensional). Lower right: Difference in September-mean sea ice concentration between the L240 and control runs (nondimensional).

Sea bounded by −70°E, 0°E, −65°N, and −35°N, since the differences would not be as clearly visible on a global plot. Since the simulations shared a common initial condition more than 60 years prior, there is no reason that they should be similar in detail; rather, the figure serves to illustrate qualitative differences between the simulations. L120 has the smallest-scale stochastic forcing, and it shows: the upper right panel of Figure 8 has significantly

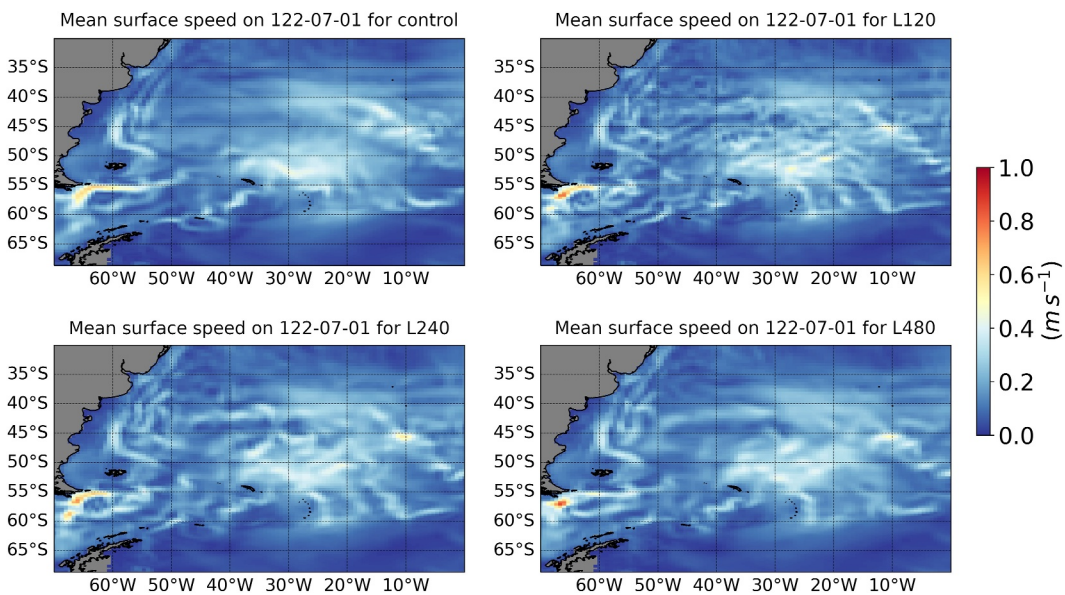

Figure 8. Daily mean sea surface speed $\sqrt{u^2 + v^2}$ on July 1 of the last year of the simulations in the region bounded by −70°E, 0°E, −65°N, and −35°N. Upper left: Control; upper right: L120; lower left: L240; lower right: L480. (m s^{-1}).

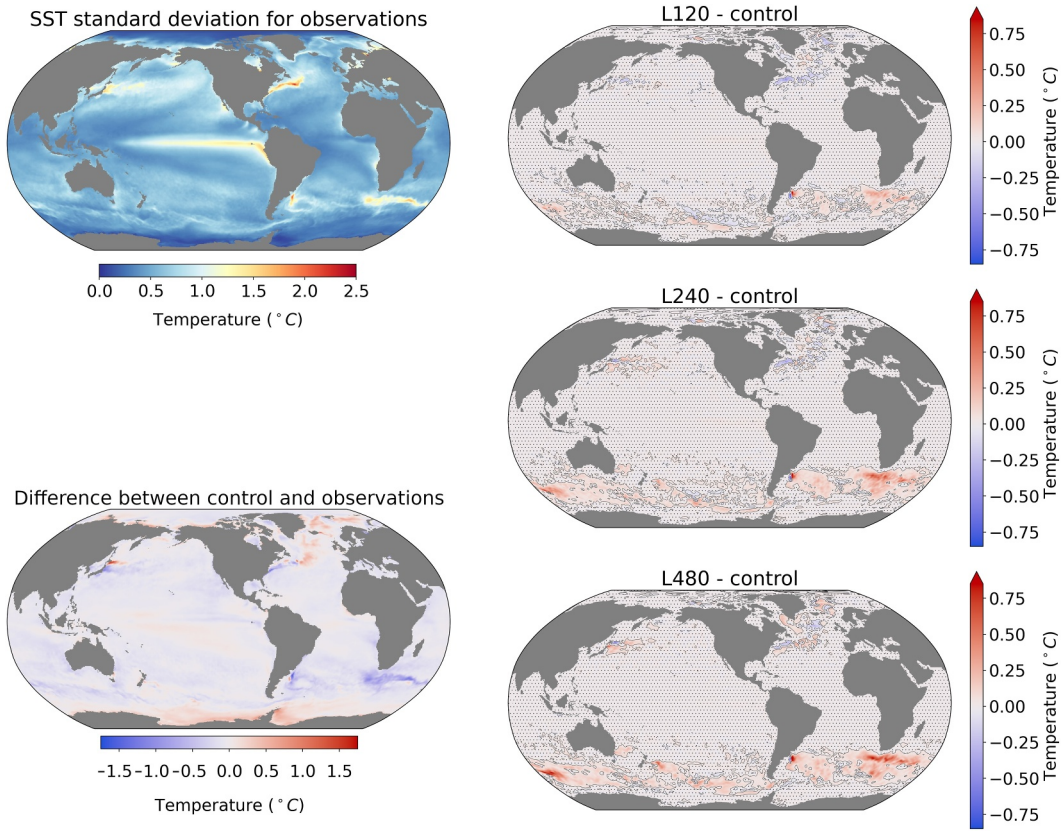

Figure 9. Top left: Standard deviation (std) of the temporal variability of SST (°C) from the OISSTv2 observational product (Reynolds et al., 2002). Center left: SST std in the control run minus the observational value. Right column: SST std in the stochastic runs minus the control run. The color scale for the right column is in the lower center of the image. In all cases the standard deviations are computed from monthly mean data with the trend and seasonal cycle removed. The stippled area in the right column denotes regions where the changes are not significant at the 95% confidence level. Differences between OISSTv2 and the control run are statistically significant everywhere that they are visibly nonzero.

more spatial variability than the other three panels. The length scales are fine enough, in fact, that they are beginning to border on being too small: some of the features in the surface speed are bordering on being not well resolved on the grid. In contrast, L240 has more spatial variability than the control run, but is much smoother than L120. Meanwhile L480 does not appear to be very different than the control. Together with Figure 2 this reinforces the idea that the length scale L_{stoch} of the stochastic forcing should be larger than the grid scale, but not too large.

4.2.1. SST Variance

Figure 9 compares the SST variability between the simulations and observations. In each case the linear trend and seasonal cycle were removed from monthly mean data before computing the standard deviations. The top left panel shows the standard deviation of the temporal variability of SST in the OISSTv2 observational product using years 1982 through 2018 (Reynolds et al., 2002). The center left panel shows the standard deviation from the control run minus the standard deviation from the observational product. The control run has too little variability over most of the globe, except in the center of the subpolar gyre in the North Atlantic and in the Ross and Weddell seas. The right column of panels in the figure shows the standard deviation from the stochastic runs minus the standard deviation from the control run. Thus, if the colors on the right panels are opposite to those of the center-left panel, then the stochastic backscatter reduces the bias. Note that the color scale on the bias in the control run is larger than the color scales in the right panel by nearly a factor of two. Statistical significance at the $p = 0.05$ level was computed using an F test (Section 2.4.2, DelSole & Tippett, 2022) for the panels in the right column, and failure to reject the null hypothesis that the standard deviations are the same is indicated by stippling.

Focusing on the right column, note that the addition of backscatter increases SST variability in broadly the same areas where the control run was deficient. The increases in SST standard deviations are large: up to 0.8 °C in places like the Agulhas return current. Nevertheless, the increase in variability is not sufficient to completely remove the variability deficit in the control run compared to observations. There are other processes besides kinetic energy backscatter that contribute to SST variability that are missing from the model; stochastic parameterizations of these other processes are needed to bring the variability up to a realistic level (e.g., Agarwal et al., 2023; Kenigson et al., 2022).

The increase in SST variability is much weaker in the L120 simulation than in the other two stochastic simulations. Although Figure 4 shows that L120 does succeed in raising the KE, the increased KE is evidently not as effective at generating SST variations as the simulations with larger-scale backscatter. In L240 and L480 the SST variability is improved significantly, especially in places where the control run had the largest deficit: the Kuroshio and its extension, the North Atlantic Current west of Grand Banks, the South Atlantic Current, and generally along the path of the Antarctic Circumpolar Current. In a coupled climate simulation this increased SST variability could have rectifying effects on, for example, midlatitude storm dynamics. Although the effect of the stochastic backscatter on SST variability is broadly positive, it does not always align precisely with the biases in the control run. This could be due to the effect of smoothing the backscatter amplitude, or also to biases in the mean location of the currents.

The addition of stochastic backscatter does not increase the SST variance everywhere. For example, east of Japan and at the Brazil-Malvinas confluence the addition of stochastic backscatter decreases SST variability in places where the control run had too much. In both locations the control run has a dipole pattern with too much variability poleward and too little equatorward, and the stochastic simulations mitigate this error. This may be due to a change in the mean position of the current in the stochastic runs.

4.2.2. SSH Variance

Figure 10 compares the SSH variability between the simulations and observations. In each case, the trend and seasonal cycle were removed from monthly mean data before computing the standard deviations. The top left panel shows the standard deviation of the temporal variability of SSH in the AVISO gridded observational product using years 1993 through 2018. The center left panel shows the standard deviation from the control run minus the standard deviation from the observational product. The control run has too little variability over much of the globe, especially along the paths of the Kuroshio extension, the North Atlantic Current, the Agulhas Return Current, and the Argentine Basin. The right column of panels shows the standard deviation from the stochastic runs minus the standard deviation from the control run. Thus, if the colors on the right panels are opposite to those of the center-left panel, then the stochastic backscatter reduces the bias. Note that the color scale on the bias in the control run is larger than the color scales in the right panel by more than a factor of two. Statistical significance at the $p = 0.05$ level was computed using an F test for the panels in the right column, and failure to reject the null hypothesis that the standard deviations are the same is indicated by stippling.

Focusing on the right column, note that the addition of backscatter increases SSH variability wherever the backscatter is active (cf. Figure 2). The increases in SSH standard deviations are larger in the southern hemisphere than in the northern hemisphere, which is consistent with the fact that the backscatter amplitude is larger in the Southern Ocean than elsewhere (Figure 2). Although the control run's deficits of SSH variability in the North Atlantic and North Pacific are reduced by the addition of stochastic backscatter, a significant deficit still remains. As with SST variability, there are other processes besides kinetic energy backscatter that contribute to SSH variability that are missing from the model; stochastic parameterizations of these other processes are needed to bring the variability up to a realistic level. Also like the SST variability, while the effect of the stochastic backscatter on SSH variability is broadly positive, it does not always align precisely with the biases in the control run. This could be due to the effect of smoothing the backscatter amplitude, or also to biases in the mean location of the currents.

The increase in SSH variability is much weaker in the L120 simulation than in the other two stochastic simulations, especially in the northern hemisphere. This could be related to the fact that smaller-scale features tend to have a smaller-amplitude footprint in SSH.

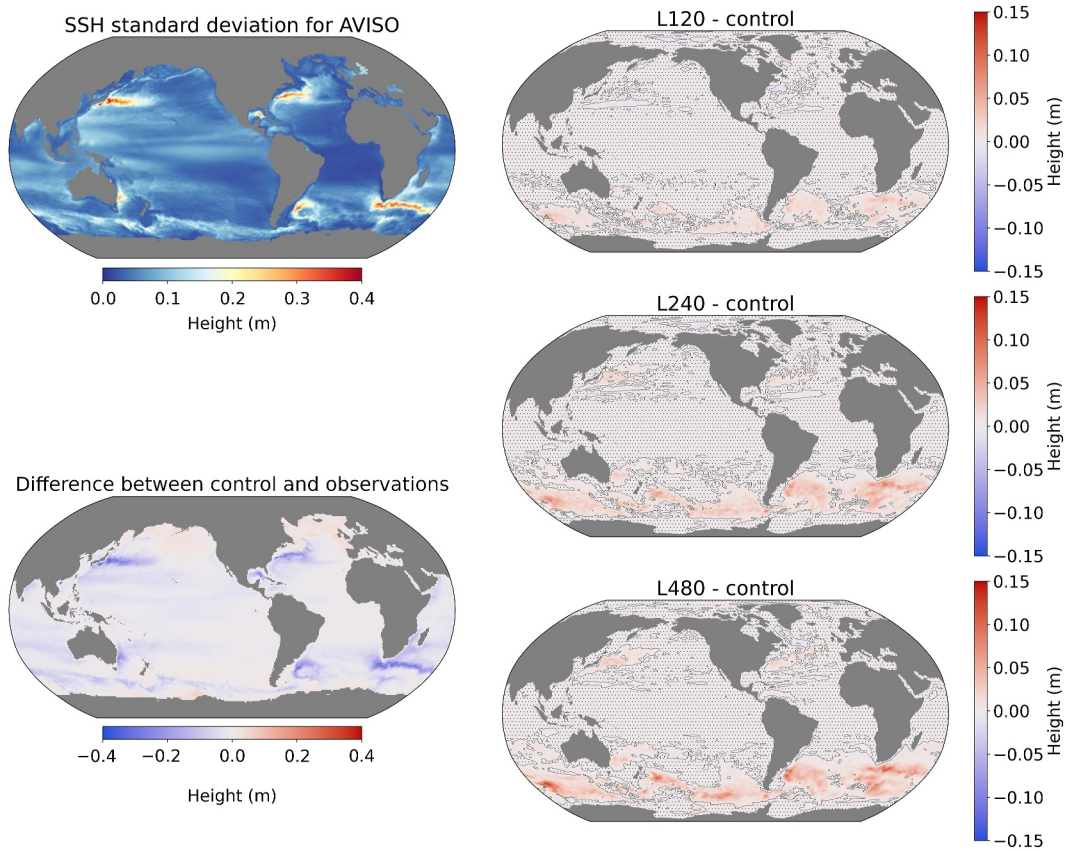

Figure 10. Top left: Standard deviation (std) of the temporal variability of SSH (m) from the AVISO gridded observational product. Center left: SSH std in the control run minus the observational value. Right column: SSH std in the stochastic runs minus the control run. The color scale for the right column is in the lower center of the image. In all cases the standard deviations are computed from monthly mean data with the trend and seasonal cycle removed. The stippled area in the right column denotes regions where the changes are not significant at the 95% confidence level. Differences between AVISO and the control run are statistically significant everywhere that they are visibly nonzero.

4.2.3. Frequency Content

The stochastic increments decorrelate rapidly, with an e-folding scale of 6 hr. The SST and SSH variability results shown above are from monthly mean data, and it is of interest to examine the frequency content of the variability induced by the stochastic forcing, in particular to assess whether the stochastic forcing is introducing too much fast variability. To that end we begin by examining the power spectrum of the daily mean SST variability at a point in Drake Passage where the stochastic forcing significantly increases the SST variance, namely at −59.2693°N, −68.6667°E. Figure 11 shows the power spectral density of daily mean SST from the control run (blue) and L240 (red), together with the 95% confidence interval of the same quantity from the OISSTv2 observational product (shaded gray). For periods less than about a week the control and L240 runs behave similarly, while the L240 run has greater power at periods from about a week to sub-decadal, excepting at a period of one year where the seasonal cycle dominates both models. Clearly the SST variability induced by the fast stochastic forcing is not primarily at short time scales. The figure also shows that at seasonal and shorter time scales (periods less than about 100 days) both the control run and L240 have significantly less variability than the observational product. This could be due, at least in part, to the fact that the observational product contains a greater range of spatial scales than the models. On seasonal and longer time scales the addition of stochastic forcing moves the model behavior up into, or even near the top of the 95% confidence interval from the observational product.

As discussed in Section 2.4, some of the kinetic energy in the stochastic increments is expected to radiate as internal waves. It is difficult to measure this directly in the model, especially since the MOM6 model currently

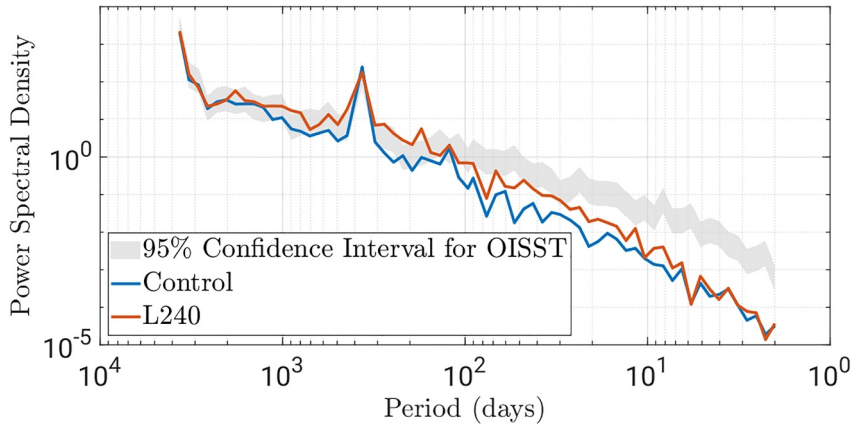

Figure 11. Power spectra of daily mean SST from the control run (blue) and L240 (red) at −59.2693°N, −68.6667°E in Drake Passage. The gray band shows the 95% confidence interval of the same quantity estimated from the OISSTv2 observational product.

lacks a vertical velocity diagnostic. As an indirect proxy we measure the temperature variance on sub-daily timescales. The sub-daily variance over a single day is computed by subtracting the daily mean temperature, squared, from the daily mean of the squared temperature; this quantity is then averaged across days. Figure 12 plots the temporal standard deviation of temperature on sub-daily time scales averaged over Southern Ocean latitudes south of 30°S. The left panel plots sub-daily temperature standard deviation as a function of depth for the control run and L240, while the right panel plots the ratio of the L240 and control run results as a function of depth. The addition of stochastic backscatter clearly does increase sub-daily temperature variability, though the increase is relatively small—on the order of 0.01℃, which amounts to an increase between 10% and 35%, depending on depth. The lack of an observational point of reference means that it is not clear if this increase is an improvement or not, but the change does not seem excessive.

5. Conclusions

We have developed a new stochastic kinetic energy backscatter scheme for OGCMs at non-eddying resolutions. The amplitude of the backscatter is proportional to the rate at which the GM parameterization removes potential energy from the resolved scales, following the GM + E parameterization of Bachman (2019). Unlike the original

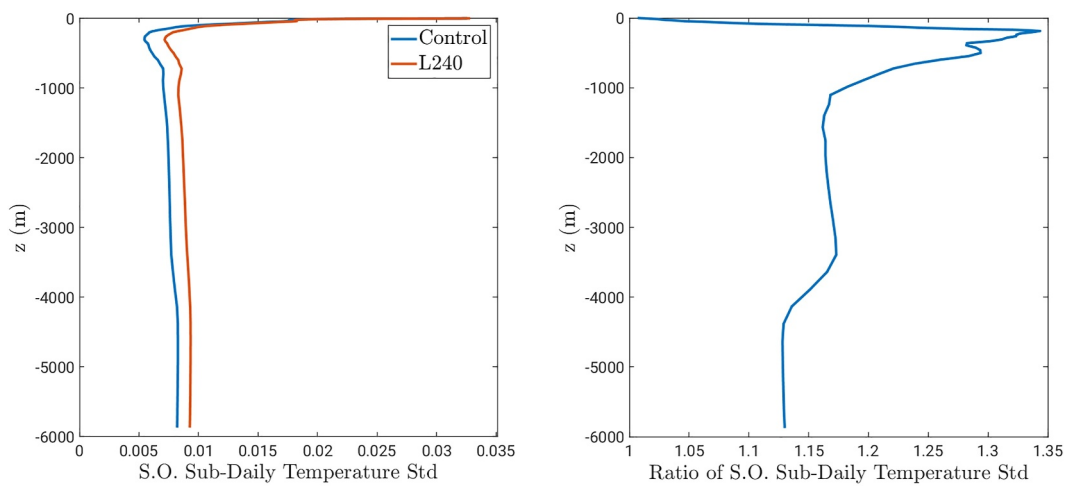

Figure 12. Left: Standard deviation of temperature on sub-daily time scales as a function of depth averaged over latitudes south of 30°S for the control run (blue) and L240 (red). The sub-daily variance is first computed at each location; this is then averaged laterally south of 30°S; the plot shows the square root of the result. Right: The ratio of the two plots in the left panel, showing that L240 has an increase in sub-daily temperature variability in the range of 10%–35%, depending on depth.

GM + E scheme, the backscatter is implemented here by adding stochastic increments to the lateral velocity field at the end of each time step. These lateral velocity increments are laterally incompressible, have a vertical structure proportional to the first surface mode (sometimes also called the "equivalent barotropic" mode), decorrelate rapidly in time, and have a tunable characteristic horizontal scale L_{stoch}.

The algorithm was implemented in the MOM6 ocean model and tested in a global forced ocean-ice configuration of CESM on a grid with a nominal resolution of $2/3°$. The parameterization has a limited effect on the model mean state, including relatively small changes to the meridional overturning circulation and a slight reduction in the zonal transport of the Antarctic Circumpolar Current. The parameterization has a profoundly positive impact on the model variability. Kinetic energy increases, as does variability of SST and SSH. The increases in SST and SSH variability are largely aligned with the regions where the control run had the largest deficit of variability compared to observations: in western boundary current extensions and along the Antarctic Circumpolar Current. The remaining deficit of variability in the parameterized model compared to observations is presumably due, at least in part, to processes other than the mesoscale eddy backscatter being parameterized here. This study has used a configuration of MOM6 that represents a snapshot in an ongoing process of developing MOM6 for use in CESM. Once that process is finalized it will be of interest to revisit the effects of this parameterization with more attention to its effect on biases of the mean state, and to compare it to alternative backscatter schemes.

The results are sensitive to the characteristic horizontal length scale L_{stoch} of the velocity increments. In our configuration setting L_{stoch} to 240 km performed better than 120 km or 480 km. The value $L_{\text{stoch}} = 240$ km is four to six times larger than the model's grid size in mid latitudes, a ballpark value that may prove useful in tuning the parameterization for other models and other grids.

This parameterization may prove useful in the context of ensemble data assimilation. Ensemble data assimilation requires a realistic level of model variability. If the model has too little variability then it tends to ignore the information content in observations, and ensemble inflation methods—which are more or less ad hoc—are required to correct an under-dispersed ensemble. As found by Grooms et al. (2015a) and Ha et al. (2015), it is generally better to correct model error by adding a stochastic parameterization than to merely account for model error by inflating an ensemble. Improvements in ensemble data assimilation enabled by the parameterization developed here may lead to improved reanalyses and to improved initialized predictions, including, for example, predictions of marine heat waves (Li & Donner, 2023). Similarly, the increase in ocean-intrinsic variability associated with this parameterization may lead to improved atmospheric variability in coupled climate models.

One area for further improvement of this parameterization is the development of a flow-aware and scale-aware theory for the fraction c of the GM work rate that should be backscattered as kinetic energy. Indeed, some theoretical support for letting the backscatter rate be proportional to the GM work rate would be valuable, as there is little theoretical support for this, or for the competing approach of letting a negative-viscosity backscatter coefficient depend on unresolved mesoscale energy (Jansen et al., 2019). The stochastic GM + E scheme could easily be turned into a stochastic GL + E scheme for use with the Greatbatch and Lamb (1990) vertical-viscosity parameterization of mesoscale eddy effects; the GL parameterization has recently been reviewed by Loose, Marques, et al. (2023). Another direction for future development is to adapt this scheme to eddying resolutions. In both that context and the context of OGCMs at coarser resolutions, it will be of interest to compare stochastic GM + E to backscatter schemes that combine GM with a negative-viscosity backscatter (Grooms, 2023; Jansen et al., 2019; Yankovsky et al., 2024). Another direction for eddying resolutions is to tie the rate of stochastic backscatter to the rate of viscous dissipation of kinetic energy in the vein of Storto and Andriopoulos (2021) or of enstrophy following Grooms (2023). Future research may also consider using Gaussian-product noise rather than Gaussian noise, since it would better represent the distribution of Reynolds stresses (Grooms, 2016). Gaussian-product noise could have a significant impact on the extreme event probabilities of the resolved dynamics (Barham & Grooms, 2019).

Appendix A: White Noise Heuristics

Let $\tilde{u}$ and $\tilde{v}$ denote the zonal and meridional components of velocity at the end of a time step but before the stochastic increments have been added. The velocity after adding the stochastic increments is

$$u = \tilde{u} + \Delta u, \tag{A1a}$$

$$v = \tilde{v} + \Delta v. \tag{A1b}$$

The mean rate of kinetic energy injection is the average of the difference between the kinetic energy before and after the stochastic increment is added, divided by the size of the time step

$$\text{Mean Rate } = \frac{1}{2\Delta t}\mathbb{E}\left[(u)^2 + (v)^2 - (\tilde{u})^2 - (\tilde{v})^2\right] \tag{A2}$$

where $\mathbb{E}$ denotes the expectation with respect to the distribution from which the stochastic velocity increments are sampled. Straightforward simplification yields the expression

$$\text{Mean Rate } = \frac{1}{\Delta t}\mathbb{E}[\tilde{u}\Delta u + \tilde{v}\Delta v] + \frac{1}{2\Delta t}\mathbb{E}\left[(\Delta u)^2 + (\Delta v)^2\right]. \tag{A3}$$

If the stochastic increments were not correlated in time, that is, if they were "white" in time or Brownian, then the cross terms would vanish and the mean rate of energy injection would depend only on the velocity increments themselves, and not on the velocity to which the increments are added. Although the velocity increments are drawn from a distribution that doesn't explicitly depend on the velocity $(\tilde{u}, \tilde{v})$, the mean of the product of the velocity and the increments is not necessarily zero. When the increments are correlated in time, the velocity $(\tilde{u}, \tilde{v})$ is correlated with the past stochastic increments, which are correlated with the current increments. Berner et al. (2009) use time-correlated increments, and therefore alter the magnitude of their backscatter to account for this correlation via heuristics discussed in their appendix. In Section 2.3 we set the amplitude of the stochastic forcing as if the mean rate of kinetic energy injection were a function only of the increments. This appendix provides heuristics in support of that approximation.

Consider a system of differential equations forced by a stochastic noise $\boldsymbol{S}$ with nonzero decorrelation time τ

$$\frac{\mathrm{d}\boldsymbol{x}}{\mathrm{d}t} = \boldsymbol{f}(\boldsymbol{x}, t) + \boldsymbol{G}(\boldsymbol{x}, t)\frac{\mathrm{d}\boldsymbol{S}}{\mathrm{d}t}. \tag{A4}$$

In many cases it can be shown that the solution of the system can be approximated by the solution of a stochastic differential equation (SDE) with Gaussian white noise forcing (i.e., Brownian increments), provided that the decorrelation time τ of the noise forcing is sufficiently small compared to the natural time scale of the unforced system. Theorems providing specific conditions under which this holds are called Wong-Zakai theorems (e.g., Pavliotis (2014) Section 5.1). that is, we may heuristically expect that solutions of the time-correlated stochastic differential equation may be approximated by solutions of

$$\mathrm{d}\boldsymbol{x} = \boldsymbol{f}(\boldsymbol{x}, t)\mathrm{d}t + \mathbf{G}(\boldsymbol{x}, t) \circ \mathrm{d}\boldsymbol{W} \tag{A5}$$

where $\boldsymbol{W}$ is a vector of independent Wiener processes. We have chosen to use a short decorrelation time of 6 hr for the stochastic velocity increments specifically for this reason: so that we can control the mean rate of kinetic energy input by approximating the noise as white in time.

Wong-Zakai theorems usually conclude that the white-noise stochastic differential equation that approximates the system with non-white noise should be interpreted in the Stratonovich rather than the Ito sense. This is indicated by the use of the $\circ$ notation in Equation A5. Under the Ito interpretation, the mean rate of kinetic energy injection is simply the mean kinetic energy of the increments divided by the time step size, which is the approximation used in this paper. The mean rate of kinetic energy injection that one would expect from the Stratonovich white-noise SDE is not, in general, the same as one would expect from the same SDE under the Ito interpretation though, because of the noise-induced drift effect in Stratonovich SDEs (cf. Jacobs, 2010). The Stratonovich SDE Equation A5 is equivalent to the following Ito SDE system, written in component form

$$\mathrm{d}x_i = \left(f_i(\boldsymbol{x}, t) + \frac{1}{2}\sum_j \sum_k G_{kj}(\boldsymbol{x}, t)\frac{\partial G_{ij}(\boldsymbol{x}, t)}{\partial x_k}\right)\mathrm{d}t + \sum_j G_{ij}(\boldsymbol{x}, t)\mathrm{d}W_j. \tag{A6}$$

The noise-induced drift that appears in the Ito version of the equation can in principle have an effect on the rate of change of kinetic energy, in addition to the effect of the white noise term.

Fortunately, in our case the noise-induced drift has no effect on the rate of change of kinetic energy. To be precise, let $\mathcal{I}$ be the set indices such that x_i is a component of velocity on the grid. The fact that the backscatter amplitude does not depend on the resolved velocity can be formalized in mathematical notation as

$$\frac{\partial G_{ij}}{\partial x_k} = 0 \text{ for } i,k \in \mathcal{I}. \tag{A7}$$

Similarly, the fact that the backscatter only appears in the velocity tendency can be formalized in mathematical notation as

$$G_{kj} = 0 \text{ for } k \notin \mathcal{I} \tag{A8}$$

where $k \notin \mathcal{I}$ indicates that x_k is not a component of velocity on the grid. Together these conspire to imply that

$$G_{kj}(\boldsymbol{x},t)\frac{\partial G_{ij}(\boldsymbol{x},t)}{\partial x_k} = 0 \text{ for } i \in \mathcal{I} \tag{A9}$$

because either $k \in \mathcal{I}$, in which case the second factor is zero, or $k \notin \mathcal{I}$, in which case the first factor is zero. We conclude that while the noise-induced drift may appear in the tracer equations, it does not appear in the velocity equations, and therefore has no direct impact on the rate of change of kinetic energy. In the SKEBS scheme of Berner et al. (2009) the backscatter amplitude does depend on the resolved velocity, so there is a noise-induced drift effect on the kinetic energy tendency, and their appendix effectively attempts to account for this drift.

Data Availability Statement

The World Ocean Atlas 2018 temperature and salinity data (WOA18 Locarnini et al., 2018; Zweng et al., 2019) used to initialize the control simulation are available for download from the official WOA18 website https://www.ncei.noaa.gov/access/world-ocean-atlas-2018/. NOAA OI SST V2 High Resolution Data set (Reynolds et al., 2002) data provided by the NOAA PSL, Boulder, Colorado, USA, from their website at https://psl.noaa.gov. SSH ((CMEMS), 2024) data provided by the E.U. Copernicus Marine Service Information https://doi.org/10.48670/moi-00148. MOM6 code, CESM case files, and diagnostic notebooks have been made publicly available (Grooms, 2025). The model output is available on the Derecho computer at /glade/campaign/cesm/development/omwg/projects/MOM6/.

Acknowledgments
The authors thank three reviewers whose comments led to an improved presentation of the research. IG and HY were supported by NSF Grant OCE 1912332. GM was supported by National Science Foundation (NSF) Grant OCE 1912420. NA was supported by the Physical Sciences Laboratory of NOAA and the Unified Forecast System Research-to-Operations project. This material is also based upon work supported by the National Center for Atmospheric Research (NCAR), which is a major facility sponsored by the NSF under cooperative agreement no. 1852977. Computing resources (https://doi.org/10.5065/qx9a-pg09) were provided by the Climate Simulation Laboratory at NCAR's Computational and Information Systems Laboratory, sponsored by the National Science Foundation and other agencies.

References

Adcroft, A., Anderson, W., Balaji, V., Blanton, C., Bushuk, M., Dufour, C. O., et al. (2019). The GFDL global ocean and sea ice model OM4. 0: Model description and simulation features. *Journal of Advances in Modeling Earth Systems*, *11*(10), 3167–3211. https://doi.org/10.1029/2019ms001726

Agarwal, N., Small, R. J., Bryan, F. O., Grooms, I., & Pegion, P. J. (2023). Impact of stochastic ocean density corrections on air-sea flux variability. *Geophysical Research Letters*, *50*(13), e2023GL104248. https://doi.org/10.1029/2023gl104248

Andrejczuk, M., Cooper, F., Juricke, S., Palmer, T., Weisheimer, A., & Zanna, L. (2016). Oceanic stochastic parameterizations in a seasonal forecast system. *Monthly Weather Review*, *144*(5), 1867–1875. https://doi.org/10.1175/mwr-d-15-0245.1

Bachman, S. D. (2019). The GM+E closure: A framework for coupling backscatter with the Gent and McWilliams parameterization. *Ocean Modelling*, *136*, 85–106. https://doi.org/10.1016/j.ocemod.2019.02.006

Bagaeva, E., Danilov, S., Oliver, M., & Juricke, S. (2024). Advancing eddy parameterizations: Dynamic energy backscatter and the role of subgrid energy advection and stochastic forcing. *Journal of Advances in Modeling Earth Systems*, *16*(4), e2023MS003972. https://doi.org/10.1029/2023MS003972

Barham, W., & Grooms, I. (2019). An eddifying Stommel model: Fast eddy effects in a two-box ocean. *Geophysical & Astrophysical Fluid Dynamics*, *113*(5–6), 505–526. https://doi.org/10.1080/03091929.2018.1464566

Berner, J., Achatz, U., Batté, L., Bengtsson, L., de la Cámara, A., Christensen, H. M., et al. (2017). Stochastic parameterization: Toward a new view of weather and climate models. *Bulletin America Meteorology Social*, *98*(3), 565–588. https://doi.org/10.1175/BAMS-D-15-00268.1

Berner, J., Shutts, G., Leutbecher, M., & Palmer, T. (2009). A spectral stochastic kinetic energy backscatter scheme and its impact on flow-dependent predictability in the ECMWF ensemble prediction system. *Journal of the Atmospheric Sciences*, *66*(3), 603–626. https://doi.org/10.1175/2008jas2677.1

Bishop, S. P., Small, R. J., Bryan, F. O., & Tomas, R. A. (2017). Scale dependence of midlatitude air–sea interaction. *Journal of Climate*, *30*(20), 8207–8221. https://doi.org/10.1175/jcli-d-17-0159.1

Blumen, W. (1972). Geostrophic adjustment. *Reviews of Geophysics*, *10*(2), 485–528. https://doi.org/10.1029/rg010i002p00485
Bodner, A. S., Fox-Kemper, B., Johnson, L., Van Roekel, L. P., McWilliams, J. C., Sullivan, P. P., et al. (2023). Modifying the mixed layer eddy parameterization to include frontogenesis arrest by boundary layer turbulence. *Journal of Physical Oceanography*, *53*(1), 323–339. https://doi.org/10.1175/jpo-d-21-0297.1
Brankart, J.-M. (2013). Impact of uncertainties in the horizontal density gradient upon low resolution global ocean modelling. *Ocean Modelling*, *66*, 64–76. https://doi.org/10.1016/j.ocemod.2013.02.004
Bryan, F. O., Hecht, M. W., & Smith, R. D. (2007). Resolution convergence and sensitivity studies with North Atlantic circulation models. Part I: The Western boundary current system. *Ocean Modelling*, *16*(3–4), 141–159. https://doi.org/10.1016/j.ocemod.2006.08.005
CMEMS, E. C. M. S. I. (2024). Global ocean gridded L 4 sea surface heights and derived variables reprocessed 1993 ongoing. https://doi.org/10.48670/moi-00148
Danabasoglu, G., Lamarque, J.-F., Bacmeister, J., Bailey, D., DuVivier, A., Edwards, J., et al. (2020). The Community Earth System Model version 2 (CESM2). *Journal of Advances in Modeling Earth Systems*, *12*(2), e2019MS001916. https://doi.org/10.1029/2019ms001916
de La Lama, M. S., LaCasce, J., & Fuhr, H. K. (2016). The vertical structure of ocean eddies. *Dynamics and Statistics of the Climate System*, dzw001. https://doi.org/10.1093/climsys/dzw001
DelSole, T., & Tippett, M. (2022). Hypothesis tests. In *Statistical methods for climate scientists* (pp. 30–51). Cambridge University Press.
Gent, P. R., & McWilliams, J. C. (1990). Isopycnal mixing in ocean circulation models. *Journal of Physical Oceanography*, *20*(1), 150–155. https://doi.org/10.1175/1520-0485(1990)020<0150:imiocm>2.0.co;2
Gent, P. R., Willebrand, J., McDougall, T. J., & McWilliams, J. C. (1995). Parameterizing eddy-induced tracer transports in ocean circulation models. *Journal of Physical Oceanography*, *25*(4), 463–474. https://doi.org/10.1175/1520-0485(1995)025<0463:peitti>2.0.co;2
Greatbatch, R. J., & Lamb, K. G. (1990). On parameterizing vertical mixing of momentum in non-eddy resolving ocean models. *Journal of Physical Oceanography*, *20*(10), 1634–1637. https://doi.org/10.1175/1520-0485(1990)020<1634:opvmom>2.0.co;2
Grooms, I. (2016). A Gaussian-product stochastic Gent-McWilliams parameterization. *Ocean Modelling*, *106*, 27–43. https://doi.org/10.1016/j.ocemod.2016.09.005
Grooms, I. (2017). Simulations of eddy kinetic energy transport in barotropic turbulence. *Phys. Rev. Fluids*, *2*(11), 113801. https://doi.org/10.1103/physrevfluids.2.113801
Grooms, I. (2023). Backscatter in energetically-constrained Leith parameterizations. *Ocean Modelling*, *186*, 102265. https://doi.org/10.1016/j.ocemod.2023.102265
Grooms, I. (2025). The stochastic GM+E closure: A framework for coupling stochastic backscatter with the Gent and Mcwilliams parameterization. *data code. Figshare*. https://doi.org/10.6084/m9.figshare.26125561
Grooms, I., Julien, K., & Fox-Kemper, B. (2011). On the interactions between planetary geostrophy and mesoscale eddies. *Dynamics of Atmospheres and Oceans*, *51*(3), 109–136. https://doi.org/10.1016/j.dynatmoce.2011.02.002
Grooms, I., & Kleiber, W. (2019). Diagnosing, modeling, and testing a multiplicative stochastic Gent-McWilliams parameterization. *Ocean Modelling*, *133*, 1–10. https://doi.org/10.1016/j.ocemod.2018.10.009
Grooms, I., Lee, Y., & Majda, A. J. (2015a). Ensemble filtering and low-resolution model error: Covariance inflation, stochastic parameterization, and model numerics. *Monthly Weather Review*, *143*(10), 3912–3924. https://doi.org/10.1175/mwr-d-15-0032.1
Grooms, I., Lee, Y., & Majda, A. J. (2015b). Numerical schemes for stochastic backscatter in the inverse cascade of quasigeostrophic turbulence. *Multiscale Modeling and Simulation*, *13*(3), 1001–1021. https://doi.org/10.1137/140990048
Grooms, I., Smith, K. S., & Majda, A. J. (2012). Multiscale models for synoptic–mesoscale interactions in the ocean. *Dynamics of Atmospheres and Oceans*, *58*, 95–107.
Ha, S., Berner, J., & Snyder, C. (2015). A comparison of model error representations in mesoscale ensemble data assimilation. *Monthly Weather Review*, *143*(10), 3893–3911. https://doi.org/10.1175/mwr-d-14-00395.1
Jacobs, K. (2010). *Stochastic processes for physicists: Understanding noisy systems*. Cambridge University Press.
Jansen, M. F., Adcroft, A., Khani, S., & Kong, H. (2019). Toward an energetically consistent, resolution aware parameterization of ocean mesoscale eddies. *Journal of Advances in Modeling Earth Systems*, *11*(8), 2844–2860. https://doi.org/10.1029/2019ms001750
Jansen, M. F., Adcroft, A. J., Hallberg, R., & Held, I. M. (2015). Parameterization of eddy fluxes based on a mesoscale energy budget. *Ocean Modelling*, *92*, 28–41. https://doi.org/10.1016/j.ocemod.2015.05.007
Jansen, M. F., Held, I. M., Adcroft, A., & Hallberg, R. (2015). Energy budget-based backscatter in an eddy permitting primitive equation model. *Ocean Modelling*, *94*, 15–26. https://doi.org/10.1016/j.ocemod.2015.07.015
Juricke, S., Danilov, S., Koldunov, N., Oliver, M., Sein, D., Sidorenko, D., & Wang, Q. (2020). A kinematic kinetic energy backscatter parametrization: From implementation to global ocean simulations. *Journal of Advances in Modeling Earth Systems*, *12*(12), e2020MS002175. https://doi.org/10.1029/2020ms002175
Juricke, S., Danilov, S., Koldunov, N., Oliver, M., & Sidorenko, D. (2020). Ocean kinetic energy backscatter parametrization on unstructured grids: Impact on global eddy-permitting simulations. *Journal of Advances in Modeling Earth Systems*, *12*(1), e2019MS001855. https://doi.org/10.1029/2019ms001855
Juricke, S., Palmer, T. N., & Zanna, L. (2017). Stochastic subgrid-scale ocean mixing: Impacts on low-frequency variability. *Journal of Climate*, *30*(13), 4997–5019. https://doi.org/10.1175/jcli-d-16-0539.1
Kenigson, J., Adcroft, A., Bachman, S., Castruccio, F., Grooms, I., Pegion, P., & Stanley, Z. (2022). Parameterizing the impact of unresolved temperature variability on the large-scale density field: 2. Modeling. *Journal of Advances in Modeling Earth Systems*, *14*(3), e2021MS002844. https://doi.org/10.1029/2021ms002844
Lacasce, J. H. (2017). The prevalence of oceanic surface modes. *Geophysical Research Letters*, *44*(21), 11–097. https://doi.org/10.1002/2017gl075430
LaCasce, J. H., & Groeskamp, S. (2020). Baroclinic modes over rough bathymetry and the surface deformation radius. *Journal of Physical Oceanography*, *50*(10), 2835–2847. https://doi.org/10.1175/jpo-d-20-0055.1
Leutbecher, M., Lock, S.-J., Ollinaho, P., Lang, S., Balsamo, G., Bechtold, P., et al. (2017). Stochastic representations of model uncertainties at ECMWF: State of the art and future vision. *The Quarterly Journal of the Royal Meteorological Society*, *143*(707), 2315–2339. https://doi.org/10.1002/qj.3094
Li, X., & Donner, S. (2023). Assessing future projections of warm-season marine heatwave characteristics with three CMIP6 models. *J. Geophys. Res.-Oceans*, *128*(5), e2022JC019253. https://doi.org/10.1029/2022jc019253
Locarnini, M., Mishonov, A., Baranova, O., Boyer, T., Zweng, M., Garcia, H., et al. (2018). World ocean atlas 2018, volume 1 (Report). *Temperature (Austin)*. Retrieved from https://archimer.ifremer.fr/doc/00651/76338/
Loose, N., Bachman, S., Grooms, I., & Jansen, M. (2023). Diagnosing scale-dependent energy cycles in a high-resolution isopycnal ocean model. *Journal of Physical Oceanography*, *53*(1), 157–176. https://doi.org/10.1175/jpo-d-22-0083.1

Loose, N., Marques, G. M., Adcroft, A., Bachman, S., Griffies, S. M., Grooms, I., et al. (2023). Comparing two parameterizations for the restratification effect of mesoscale eddies in an isopycnal ocean model. *Journal of Advances in Modeling Earth Systems*, *15*(12), e2022MS003518. https://doi.org/10.1029/2022ms003518

Marques, G. M., Shao, A. E., Bachman, S. D., Danabasoglu, G., & Bryan, F. O. (2023). Representing eddy diffusion in the surface boundary layer of ocean models with general vertical coordinates. *Journal of Advances in Modeling Earth Systems*, *15*(6), e2023MS003751. https://doi.org/10.1029/2023ms003751

Marshall, D. P., Maddison, J. R., & Berloff, P. S. (2012). A framework for parameterizing eddy potential vorticity fluxes. *Journal of Physical Oceanography*, *42*(4), 539–557. https://doi.org/10.1175/jpo-d-11-048.1

Moreno-Chamarro, E., Caron, L.-P., Loosveldt Tomas, S., Vegas-Regidor, J., Gutjahr, O., Moine, M.-P., et al. (2022). Impact of increased resolution on long-standing biases in highresmip-primavera climate models. *Geoscientific Model Development*, *15*(1), 269–289. https://doi.org/10.5194/gmd-15-269-2022

O'Kane, T. J., Fiedler, R., Collier, M. A., & Kitsios, V. (2023). Ocean model response to stochastically perturbed momentum fluxes. *Journal of Climate*, *36*(6), 1895–1922. https://doi.org/10.1175/jcli-d-21-0796.1

Pavliotis, G. A. (2014). *Stochastic processes and applications*. Springer.

Redi, M. H. (1982). Oceanic isopycnal mixing by coordinate rotation. *Journal of Physical Oceanography*, *12*(10), 1154–1158. https://doi.org/10.1175/1520-0485(1982)012<1154:oimbcr>2.0.co;2

Reynolds, R. W., Rayner, N. A., Smith, T. M., Stokes, D. C., & Wang, W. (2002). An improved in situ and satellite SST analysis for climate. *Journal of Climate*, *15*(13), 1609–1625. https://doi.org/10.1175/1520-0442(2002)015<1609:aiisas>2.0.co;2

Roach, L. A., Dörr, J., Holmes, C. R., Massonnet, F., Blockley, E. W., Notz, D., et al. (2020). Antarctic sea ice area in CMIP6. *Geophysical Research Letters*, *47*(9), e2019GL086729. https://doi.org/10.1029/2019gl086729

Rocha, C. B., Young, W. R., & Grooms, I. (2016). On Galerkin approximations of the surface active quasigeostrophic equations. *Journal of Physical Oceanography*, *46*(1), 125–139. https://doi.org/10.1175/jpo-d-15-0073.1

Schumann, U. (1995). Stochastic backscatter of turbulence energy and scalar variance by random subgrid-scale fluxes. *Proceedings of the Royal Society of London. Series A: Mathematical and Physical Sciences*, *451*(1941), 293–318.

Smith, R. D., Maltrud, M. E., Bryan, F. O., & Hecht, M. W. (2000). Numerical simulation of the North Atlantic Ocean at 1/10. *Journal of Physical Oceanography*, *30*(7), 1532–1561. https://doi.org/10.1175/1520-0485(2000)030<1532:nsotna>2.0.co;2

Stanley, Z., Grooms, I., Kleiber, W., Bachman, S., Castruccio, F., & Adcroft, A. (2020). Parameterizing the impact of unresolved temperature variability on the large-scale density field: Part 1. Theory. *Journal of Advances in Modeling Earth Systems*, *12*(12), e2020MS002185. https://doi.org/10.1029/2020ms002185

Storto, A., & Andriopoulos, P. (2021). A new stochastic ocean physics package and its application to hybrid-covariance data assimilation. *The Quarterly Journal of the Royal Meteorological Society*, *147*(736), 1691–1725. https://doi.org/10.1002/qj.3990

Tsujino, H., Urakawa, S., Nakano, H., Small, R. J., Kim, W. M., Yeager, S. G., et al. (2018). JRA-55 based surface dataset for driving ocean–sea-ice models (JRA55-do). *Ocean Modelling*, *130*, 79–139. https://doi.org/10.1016/j.ocemod.2018.07.002

Williams, P., Howe, N., Gregory, J., Smith, R., & Joshi, M. (2016). Improved climate simulations through a stochastic parameterization of ocean eddies. *Journal of Climate*, *29*(24), 8763–8781. https://doi.org/10.1175/jcli-d-15-0746.1

Williams, P. D. (2012). Climatic impacts of stochastic fluctuations in air–sea fluxes. *Geophysical Research Letters*, *39*(10), L10705. https://doi.org/10.1029/2012gl051813

Yankovsky, E., Bachman, S., Smith, K. S., & Zanna, L. (2024). Vertical structure and energetic constraints for a backscatter parameterization of ocean mesoscale eddies. *Journal of Advances in Modeling Earth Systems*, *16*(7), e2023MS004093. https://doi.org/10.1029/2023ms004093

Yassin, H., & Griffies, S. M. (2022). On the discrete normal modes of quasigeostrophic theory. *Journal of Physical Oceanography*, *52*(2), 243–259. https://doi.org/10.1175/jpo-d-21-0199.1

Zanna, L., & Bolton, T. (2020). Data-driven equation discovery of ocean mesoscale closures. *Geophysical Research Letters*, *47*(17), e2020GL088376. https://doi.org/10.1029/2020gl088376

Zweng, M., Reagan, J., Seidov, D., Boyer, T., Locarnini, M., Garcia, H., et al. (2019). World ocean atlas 2018, volume 2 (Report). *Salinity*. Retrieved from https://archimer.ifremer.fr/doc/00651/76339/